

# Tuning the mechanical properties of CrCoFeMnNi high entropy alloy via cold spray additive manufacturing associated with heat treatment

Bemechal Tsegaye Mengiste<sup>a</sup>, Ali Arab<sup>b, \*\*</sup>, Yansong Guo<sup>a</sup>, Yinze Lei<sup>a</sup>, Xiaoshuai Li<sup>a</sup>, Pengwan Chen<sup>a</sup>, Jing Xie<sup>a,\*</sup>

<sup>a</sup> State Key Laboratory of Explosion Science and Technology, Beijing Institute of Technology, Beijing, 100081, China

<sup>b</sup> Multidisciplinary Center for Infrastructure Engineering, Shenyang University of Technology, Shenyang, 110870, China



## ARTICLE INFO

**Keywords:**  
Cold spray  
High entropy alloy  
Deformation behavior  
Anisotropic properties

## ABSTRACT

The CoCrFeMnNi high entropy alloy (HEA) is the most studied HEA because of its excellent combination of strength and ductility. However, despite the advantage of CoCrFeMnNi HEA, its application is limited owing to its low yield strength. In this study, an emerging cold spray additive manufacturing technique was applied to fabricate a bulk CrCoFeMnNi high entropy alloy to improve the yield strength of CrCoFeMnNi. The paper presented an experimental investigation of the microstructure and mechanical properties of the as-sprayed and heat-treated CrCoFeMnNi high entropy alloy samples under compressive loading conditions at different strain rates. The microstructural analysis of the as-sprayed samples exhibited undeformed particles, numerous refined grains, and an interparticle incomplete interface. Post-heat treatment was applied to tune inter-particle bonding and ductility. Quasi-static compression tests (at  $0.001\text{ s}^{-1}$ ) and dynamic impact tests (up to  $3900\text{ s}^{-1}$ ) were carried out on the as-sprayed and heat-treated samples along the printing direction (vertical samples) and perpendicular to the printing direction (horizontal samples). The extraordinary mechanical properties of the as-sprayed vertical samples reached a yield strength of  $\sim 1036.6\text{ MPa}$  and an ultimate compressive strength of  $\sim 1117.8\text{ MPa}$  at a strain deformation of 10.1%. The as-sprayed horizontal samples had a yield strength of  $\sim 1033.1\text{ MPa}$  and an ultimate compressive strength of  $\sim 1102\text{ MPa}$  at a strain of 5.6%. Thus, the as-sprayed (vertical and horizontal) samples showed mechanical anisotropic properties. Further, the as-sprayed samples showed brittle behavior. However, as-sprayed samples exhibit high ductility, up to 70%, and high plastic deformation after heat treatment. The deformation mechanism of as-sprayed and heat-treated samples is dominated by deformation twinning. This work showed excellent yield and ultimate compressive strength compared to other CrCoFeMnNi high entropy alloy manufacturing methods.

## 1. Introduction

High entropy alloys (HEAs) are emerging novel alloys, mainly constructed from five or more principal elements in an equiatomic or near equiatomic mixture [1]. The equiatomic mixture is believed to produce four core effects in the solution, i.e., high entropy effect, sluggish diffusion, lattice distortion, and cocktail effect, that help the formation of better microstructure and properties [2]. In addition, the multi-component mixing helps to prevent the formation of intermetallic phases rather than promoting the formation of a solid solution structure. Unlike conventional alloys, HEAs have excellent physical and mechanical properties, including high hardness, super-conductivity, wear

resistance, corrosion resistance, and thermal stability [3,4]. Among the different HEAs, the extensively studied alloy is CrCoFeMnNi HEA, exhibiting a single-phase FCC solid solution with excellent damage tolerance, relatively low yield stress, superior ductility, and good fracture toughness at ambient and cryogenic temperatures [5]. Owing to the extraordinary behavior of CrCoFeMnNi HEA, different fabrication techniques have been used, such as casting [6], direct energy deposition [7,8], selective laser melting [9], laser powder-bed fusion [10,11], arc cladding [12], cold spray deposition [13–15], etc., to explore its industrial application.

Cold spray additive manufacturing (CSAM) is a new emerging solid-state powder deposition technology for coating, repairing, and near-net

\* Corresponding author.

\*\* Corresponding author.

E-mail addresses: [aarab1362@gmail.com](mailto:aarab1362@gmail.com) (A. Arab), [jxie@bit.edu.cn](mailto:jxie@bit.edu.cn) (J. Xie).

shape manufacturing. CSAM is a promising method to fabricate high-strength CrCoFeMnNi HEA. CSAM uses high-pressure carrier gases (usually N<sub>2</sub>, He, and air) to accelerate the microscopic powder particles on the substrate. Upon impact, powder particles are plastically deformed, and as the incoming particles continue to impact with the previously deposited particles, resulting in localized temperature rise (thermal softening) and adiabatic shear instability at the contact region, which are the necessary conditions for metallurgical bonding in the particle interfaces. The particle temperature and critical velocity assist in creating particle bonding through the induced severe plastic deformation [16,17], excess kinetic energy [16], adiabatic shear instability (strain localization) [18], and localized melting [19]. As powders are deposited layer by layer, resulting in dense coating, hard bonds, and finally consolidated and built freestanding components. Due to its unique manufacturing merits, CSAM has been increasingly used in many industries, including aerospace, energy, and military [20,21]. Besides, CSAM was used for the deposition of various materials, including high entropy alloys [22,23]; metallic glass alloys [24–26]; Aluminum [27, 28]; Zinc [29]; Copper [30–32]; Titanium [33–37]; Nickel and its alloys [38,39]; Steel [40–42]; Magnesium [43–45]; and in some cases cermet powders [46–48].

Nowadays, a few HEAs have been deposited via CSAM; among them, CrMnFeCoNi HEA has received the most attention owing to its good thermal stability and printability [49]. Yin et al. reported the first tribological properties of the CSed FeCoNiCrMn HEA coating on an Al substrate with a tough surface, no phase change of CSed particles, low porosity, and a lower wear rate [49]. Xu et al. reported the incomplete interparticle interfaces of 3 mm thick freestanding cold-sprayed FeCoCrNiMn HEA. The post-heat treatment method promoted recrystallization and grain growth in the CSed HEA [50]. Furthermore, Nikbakht et al. studied the deformation behavior and bonding characteristics of cold-sprayed CrMnFeCoNi HEA [14]. Another study by Ahn et al. examined the microstructure and mechanical properties of CSed CoCrFeMnNi HEA Coating and various heat treatments. The coated layer showed a heterogeneous microstructure, ultra-fine grains within the interfaces, and coarse grains inside the particles. The hardness of the CSed coating layer, in which the nano-indentation test showed 10.9 GPa, is approximately three times higher than that of the conventional cast HEA; the reason could be the dislocation density and ultra-fine grain formation [23]. In addition, Lehtonen et al. studied CrFeNiMn coating on Fe52 steel substrate for nuclear industries application instead of stainless-steel coatings. The coating layer resulted in a single-phase structure and high hardness with coating thicknesses of 230–490 µm and porosity (3%–10%) [51]. Generally, CSAM often exhibits ultra-thick coatings, high bond strength and hardness, high corrosion resistance, low residual stresses, no phase change of powder, quality products (near-net-shape), and illimitable product size can be processed [18]. Nevertheless, CSAM products have many drawbacks, such as high microporosities, uncrystallized grains, rough surface, and poor ductility, resulting in unfavorable mechanical properties for industrial applications.

This work successfully printed bulk CrMnFeCoNi HEA via CSAM, followed by heat treatment. The paper aims to study the mechanical properties of the as-sprayed CrMnFeCoNi HEA. Besides, the effect of build orientation on the microstructure and compressive behaviors of vertical samples (printing direction) and horizontal samples (perpendicular to printing direction) under different strain rates. Furthermore, the anisotropic mechanical properties, deformation behaviors, and fracture analysis have been investigated.

## 2. Experimental procedures

### 2.1. Powder material and substrate

Equiatomic CoCrFeMnNi HEA powder (Beijing Yanbang New Material Technology Co. Ltd., China) was purchased and used as a feedstock

for cold spray deposition, Fig. 1(a) shows a spherical shape, Fig. 1(b) depicts near equiatomic. The powder size distribution was 15–53 µm (a d<sub>50</sub> value of 29.351 µm). The chemical composition of the powder is shown in Fig. 1(b). Al 6061 alloy substrate (5 mm thickness) was used for CS deposition. Prior to deposition, the substrate was grit-blasted using an alumina grit blasting pressure of 3 bar.

### 2.2. Cold spray process

The CrCoFeMnNi HEA powder was cold sprayed on Al6061 substrate using the cold spraying facility of Impact Innovations (GmbH, Germany) using nitrogen as processing gas. The gas temperature and pressure were set at 600 °C and 4.2 MPa, respectively; the gas flow, the scan velocity, and the standoff distance from the nozzle exit to the substrate surface were set at 100 m<sup>3</sup>/h, 30 mm/s, and 25 mm, respectively. About 70 mm × 70 mm × 8 mm freestanding CrMnFeCoNi HEA plate was successfully printed, as shown in Fig. 2 (a).

### 2.3. Sintering process

The sintering mechanism of CrCoFeMnNi HEA is well discussed by Zhang et al. [52]; the melting point starts at 1300 °C and reaches up to 1350 °C. Therefore, the sintering temperature is suggested to be below 1300 °C. This work follows the same sintering process as Zhang et al. [52]. The as-spared samples were heat treated at temperatures of 600 °C, 900 °C, 1100 °C, 1200 °C, and 1250 °C in a muffle furnace for 1 h with a heating rate of 10 °C/min, followed by furnace cooling. The sintered samples showed slight shrinkage due to oxidation when the sintering temperature was 1250 °C. Sintering aims to bond the deformed and undeformed powders together, activate grain growth, and improve the mechanical plasticity of the samples. The density of the as-sprayed deposit was measured before and after sintering by a density balance (Sartorius SQP).

### 2.4. Microstructure characterization

Before microstructural characterization, the as-sprayed CrMnFeCoNi HEA deposit was carefully sectioned from the substrate via a Wire Electrical Discharging Machine (EDM). Then, the piece of samples was cut using EDM (5 mm × 5 mm × 2 mm) from the as-sprayed deposit for microstructural characterization. Both the as-sprayed and sintered samples followed the standard sample preparation process. Hence, the CrCoFeMnNi HEA deposit is unsuitable for chemical etchants, so we used the standard sample preparation procedure of ion polishing methods. The prepared samples have been ground mechanically using 400#, 1000#, 2000#, and 5000# water sanding papers to obtain a smooth and delicate surface, and then polished by Leica EMRES102 argon ion polishing instrument, with an applied voltage of 5 KeV, 4 KeV, and 3 KeV for 1 h for each polishing process. The sample surface with bright and smooth surfaces was then examined by an optical microscope (OM), scanning electron microscopy (SEM), and electron backscatter diffraction (EBSD). The fracture morphology was observed by SEM.

To identify the phase structure and crystallinity of the CrMnFeCoNi HEA powder, the as-sprayed and sintered deposit was back-mounted in a Bruker cavity holder, X-ray diffractometer (Bruker D8 Focus, Germany). The XRD data were collected in a 2 θ range of 40 ° to 100 ° with Co Kα radiation source ( $\lambda = 0.178897 \text{ nm}$ ), voltage of 35 kV, current of 40 mA, and scan speed of 2°/min. The principal element and their distribution of the powder, the as-sprayed, and sintered deposit was performed using an energy-dispersive X-ray spectroscopy (Oxford Instruments, UK) equipped with an SEM system. An OM image was used to measure the porosity of the as-sprayed and sintered deposits using ImageJ software (seen in Fig. 5). At least ten images were used to estimate the average porosity value. The grain structure and the microstructures of as-sprayed, sintered, and deformed samples were investigated by EBSD (JSM7200FESEM, Japan) and SEM, FlexSEM-1000II (Oxford instrument,

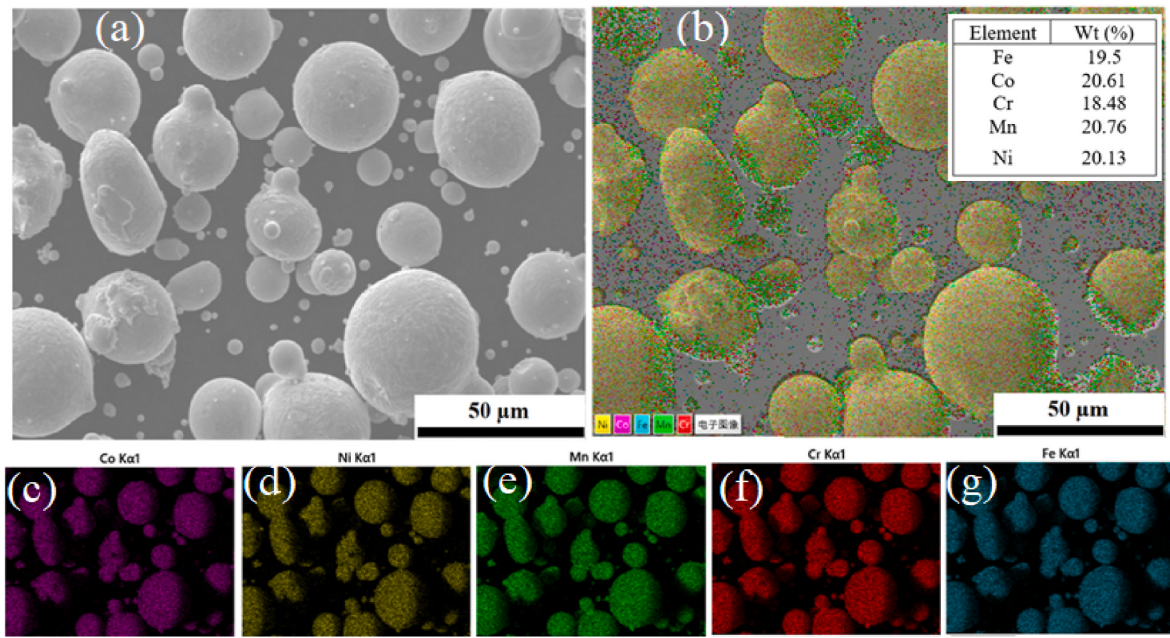


**Fig. 1.** CrCoFeMnNi high entropy alloy powder characteristics, (a) SEM image, (b–g) EDS maps of constituent elements.

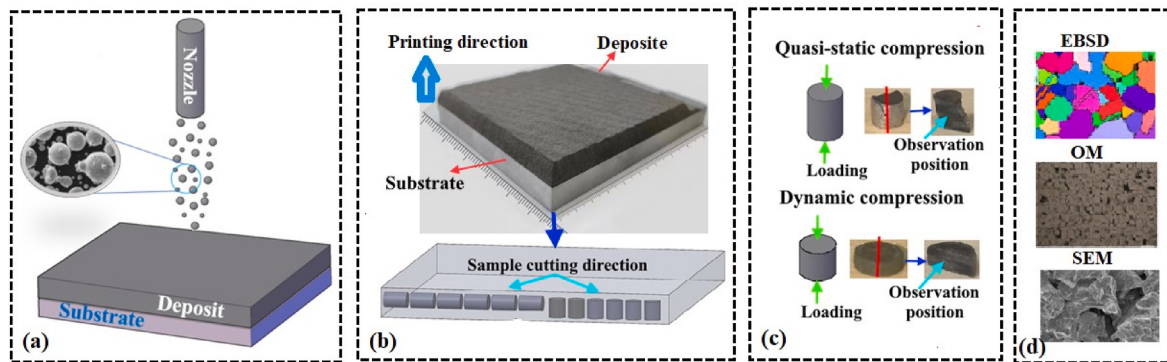


**Fig. 2.** The processing sequence of the cold spraying process (a) cold spraying, (b) the as-sprayed deposit and cutting design, (c) uniaxial compression tests, and (d) microstructure characterization.

UK). The setting for EBSD measurements as velocity super, Voltage 20kv, and Current 6.4 nA. The microhardness of the as-sprayed and sintered deposit was conducted at room temperature using a digital microhardness tester at a load of 2.942 N and a dwell time of 15 s. At least ten Vickers hardness tests were evaluated for each sample.

## 2.5. Compression tests

### 2.5.1. Quasi-static compression test

The cylindrical samples with  $6 \text{ mm} \times \varnothing 4 \text{ mm}$  for quasi-static and  $4 \text{ mm} \times \varnothing 4 \text{ mm}$  for dynamic compression test were prepared via wire cutting machine (EDM) from the as-sprayed deposit. We prepared two different orientation samples to study the deformation behavior of the as-sprayed deposits, as shown in Fig. 2(b). The first was the vertical samples, extracted along the print direction ( $0^\circ$ ), and the second was horizontal samples, extracted perpendicular ( $90^\circ$ ) to the printing direction. Room temperature quasi-static compression behavior was tested by using a standard GB/T7314-2017 metallic materials testing system with a strain rate of  $1 \times 10^{-3} \text{ s}^{-1}$ . An electronic universal material testing machine, (INSTRON5985, US) was used for this quasi-static test. At least three replicate tests were performed for the quasi-static testing to confirm the reputability of the result for both as-

sprayed and sintered samples.

### 2.5.2. Dynamic compression test

The dynamic behavior of the as-sprayed and sintered samples was carried out by the split Hopkinson pressure bar (SHPB) facility at room temperature. Fig. 3 illustrates the basic SHPB setup. SHPB comprises a gas gun, a striker bar ( $\varnothing 14\text{mm} \times 200\text{ mm}$ ), an incident bar ( $\varnothing 14\text{ mm} \times 1200\text{ mm}$ ), and a transmission bar ( $\varnothing 14\text{ mm} \times 1200\text{ mm}$ ); all bars are made of maraging steel. The sample was sandwiched between the incident and transmitted bars. Five replicate tests were performed for the dynamic compressive testing for both as-sprayed and sintered samples.

The sample's strain rate ( $\dot{\epsilon}$ ), stress ( $\sigma$ ) and strain ( $\epsilon$ ) were calculated from the one-dimensional stress-wave principle using the following equations [53,54]:

$$\dot{\epsilon}(t) = \frac{2C_o}{l_s} \epsilon_r \quad (1)$$

$$\epsilon(t) = \frac{2C_o}{l_s} \int_0^t \epsilon_r dt \quad (2)$$

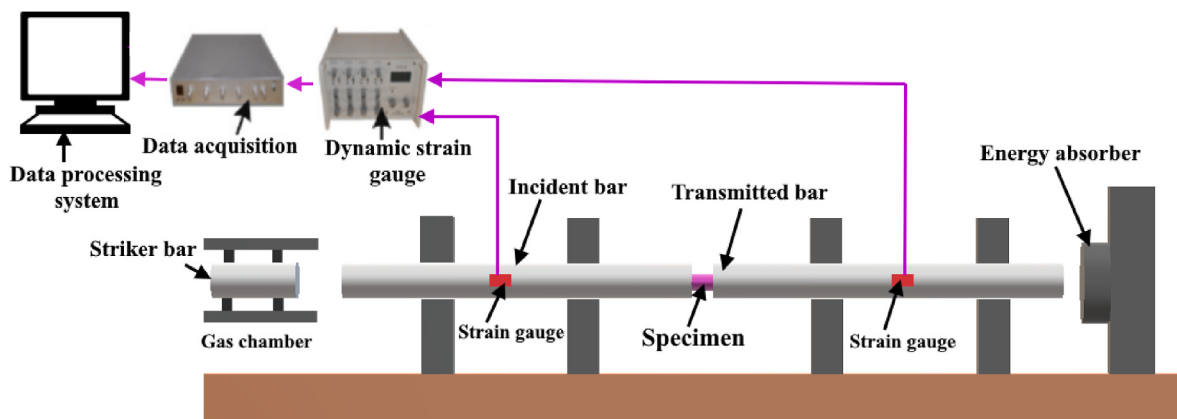


Fig. 3. Common compression split Hopkinson pressure bar setup.

$$\sigma(t) = \frac{AE}{A_o} \epsilon_t \quad (3)$$

where E is the elastic modulus of the bar, A is the cross-sectional area of the bar, and  $C_o$  is the sound speed of the bars,  $l_s$  is the length of the sample,  $A_o$  is the cross-sectional area of the sample,  $\epsilon_t$  is strain obtained from reflected, and  $\epsilon_t$  represent the strain obtained from the transmitted wave.

The true stress-strain curve was calculated by the following equation [54]:

$$\sigma_T = (1 - \epsilon) \sigma \quad (4)$$

$$\epsilon_T = -\ln(1 - \epsilon) \quad (5)$$

where  $\sigma$  is the engineering stress,  $\epsilon$  is the engineering strain,  $\sigma_T$  is the true stress, and  $\epsilon_T$  is the true strain.

### 3. Results

#### 3.1. Microstructure analysis

Fig. 4 shows the phase structure of the CoCrFeMnNi HEA powder, as-sprayed, and sintered deposit. All three main peaks (111), (200), and (220) are single-phase FCC ( $a_0 = 3.6 \text{ \AA}$ ) structures that occurred at the same position, implying that there is no phase transformation during

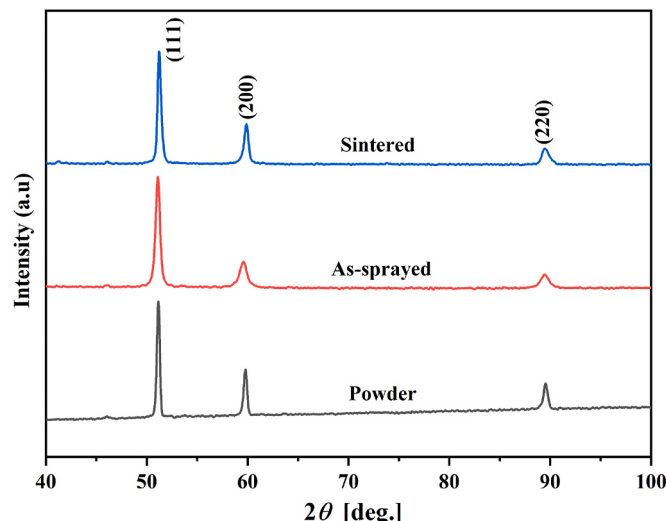


Fig. 4. XRD patterns of CrCoFeMnNi HEA powder, as-sprayed, and sintered states.

cold spraying and sintering at  $1250^\circ \text{C}$  for 1 h. The cold-sprayed XRD pattern shows peak broadening as the result of residual stresses. The microstrain ( $\epsilon$ ) and crystallite size (d) of the powder, as-sprayed, and sintered samples were estimated from the true XRD peaks broadening by using the Williamson-Hall plot method [55,56]. The true peak broadening  $\beta$ , microstrain ( $\epsilon$ ), and the crystallite size (d) can be related as:

$$\beta \cos \theta_B = \frac{\kappa \lambda}{d} + \epsilon 4 \sin \theta_B \quad (6)$$

Where  $\beta$  (in radians) is the broadening at half maximum intensity,  $\theta_B$  is Bragg's angle of the peak,  $\lambda$  is the wavelength of the CoK $\alpha$  radiation source (0.178897 nm), and  $\kappa$  is a constant (0.9).

The microstrain ( $\epsilon$ ) and crystallite size (d) were automatically evaluated from XRD peaks, the full width at half maximum (FWHM) algorithm in Origin Pro software. Then, using the peaks fit in a linear plot, the slope of the fit represents a measure of microstrain. By using Eq. (6), the microstrain of powder, as-sprayed, and sintered HEA samples of the three FCC peaks can be estimated as  $3.62 \times 10^{-3}$ ,  $6.61 \times 10^{-3}$ ,  $1.01 \times 10^{-3}$  respectively. The as-sprayed samples showed large microstrain, i.e.,  $6.61 \times 10^{-3}$  compared to CoCrFeMnNi HEA powder, and sintered samples due to severe plastic deformation and residual stress developed during cold spraying. Other studies also reported near similar results in HEA, supporting this analysis [56,57]. Further, the powder's crystallite size (d), as-sprayed, and sintered samples of the three FCC peaks are 15.5 nm, 8.3 nm, and 45.5 nm, respectively. The sintered samples showed higher crystallite size due to grain growth, whereas the cold spray showed the smallest crystallite size compared to HEA powder due to grain refinement during cold spraying.

Fig. 5 shows the OM micrographs (unetched) of the CrCoFeMnNi HEA as-sprayed and sintered samples. Most of the grains have a spherical shape. However, a few elongated particle shapes were also observed in the sprayed samples developed during CS plastic deformation, as shown in Fig. 5(a), marked by white arrows.

After sintering at  $1250^\circ \text{C}$  for 1 h, the spherical grains and inter particles interface migrated towards each other and partially disappeared, resulting in grain growth with spherical pores, as seen in Fig. 5 (b). The porosity of the as-sprayed samples was measured to be  $11 \pm 0.4\%$ . However, the sintered sample porosity was reduced to  $4 \pm 0.2\%$ .

Fig. 6 presents the cold-sprayed EBSD microstructure of the deposit observed from the printing direction, YZ plane (TD), and perpendicular to the printing direction, XY plane (ND), which shows slightly different grain distributions as shown in Fig. 6(a<sub>1</sub>) and (b<sub>1</sub>), marked by a circle. Fig. 6(a and b) displays the distorted crystal lattice owing to high strain and numerous refined and elongated grains in Fig. 6(a<sub>1</sub>, b<sub>1</sub>), implying that the more particles deformation and recrystallization. High-velocity impact results in severe particle plastic deformation, leading to

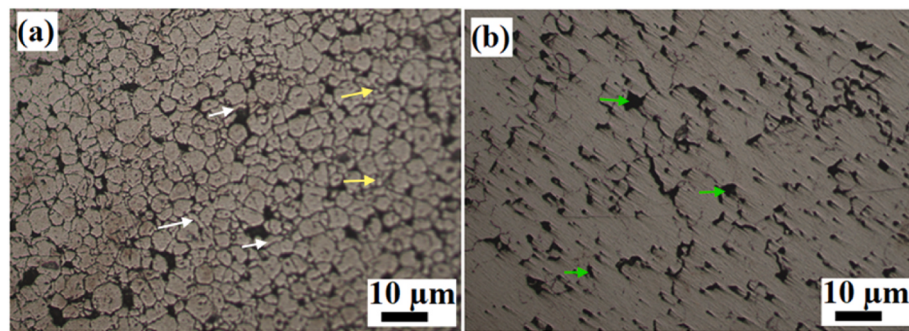


**Fig. 5.** Cold sprayed CrCoFeMnNi HEA OM images (unetched) (a) as-sprayed, (b) sintered at 1250 °C for 1 h (white, yellow, and green arrows show elongated grains, refined grains, and spherical pores, respectively). (For interpretation of the references to color in this figure legend, the reader is referred to the Web version of this article.)

significant compression and flattening in the printing direction. The step size for EBSD (Fig. 6) is 0.5 μm. The worst IQ map shown in Fig. 6(a and b) results from residual strain induced by severe plastic deformation of the particles and extremely high dislocation density developed within the interparticle interfaces.

The grain structure of the as-sprayed HEA displays numerous refined grains, as seen in Fig. 6(a<sub>1</sub>, b<sub>1</sub>), due to incomplete particle deformation and poor recrystallization of particles during CS deposition. Few elongated grains (the circled region in Fig. 6(a<sub>1</sub>, b<sub>1</sub>)) are retained in the grain structure due to less plastic deformation. The average grain size of the as-sprayed horizontal and vertical samples, as shown in Fig. 6 (a<sub>3</sub>, b<sub>3</sub>), were 3.8 μm and 3.7 μm, respectively. The average grain size of the vertical sample is 3.7 μm, which is less than the horizontal sample (3.8 μm). Refined grains are essential as a strengthening mechanism by blocking dislocation motion. The KAM map shown in Fig. 6(a<sub>2</sub>, b<sub>2</sub>) displays almost green and little red, indicating that the as-sprayed deposit exhibits severe plastic deformation and higher dislocation density. KAM measures plastic deformation and grain orientation difference using color translation from low KAM 0 ° (blue) to maximum KAM 5 ° (red) [58]. KAM studies the recovery and recrystallization of plastically deformed materials. Low KAM values (<1.5°) represent recrystallization. The higher KAM values are found in the grain boundaries, interparticle interfaces, and micropores [58].

Based on the grain boundary classification methods, grain boundaries are divided into low-angle grain boundary (LAGBs) angles less than 15 ° and high-angle grain boundaries (HAGBs) angles higher than 15 °. The calculated values of LAGBs and HAGBs shown in the misorientation angle distribution histogram in Fig. 6(a<sub>4</sub>) of the horizontal as-sprayed HEA are 68.4% and 31.6% respectively. Similarly, the LAGBs and HAGBs shown in the misorientation angle distribution histogram Fig. 6 (b<sub>4</sub>) of the vertical as-sprayed samples are 66.09% and 33.91%, respectively.

Fig. 7 shows the microstructures and corresponding EDS maps of the as-sprayed sample. The distribution of elements such as Co, Cr, Mn, Fe, and Ni are uniform, and each element's atomic and weight percentage is nearly equal after CS, as shown in Fig. 7(c), and no impurities are observed in the as-sprayed sample.

### 3.2. Effect of heat treatment on microstructure

The as-sprayed sample commonly results in weak metallurgical and interfacial bonding between the deformed powder interface, as discussed in section 3.1. Therefore, heat treatment at different temperatures was applied to improve the interparticle bonding and remove the porosity of the as-sprayed samples. As expected, the interparticle bonding and porosity are highly improved due to grain recrystallization and growth at a sintering temperature of 1250 °C.

Fig. 8 shows the EBSD map of the sintered CrCoFeMnNi HEA sample at 1250 °C. Fig. 8(a) shows that the IQ map displays a clear, large

equiaxed grain, including grain boundary, spherical pores, and micro-pores inside grains. The observed micropores were developed due to the incomplete particle bonding during CS deposition. Fig. 8(b) shows the grain structure of the sintered sample. The ultrafine grain, elongated grains, and highly strained regions of the as-sprayed sample shown in Fig. 6 completely disappeared upon sintering, resulting in large equiaxed grain structures being grown, as seen in Fig. 8 (b). Further, the KAM map shown in Fig. 8(c) displays dominantly blue, indicating that the as-sprayed sample was fully recrystallized. Static recovery releases the stored residual strain seen in the as-sprayed sample.

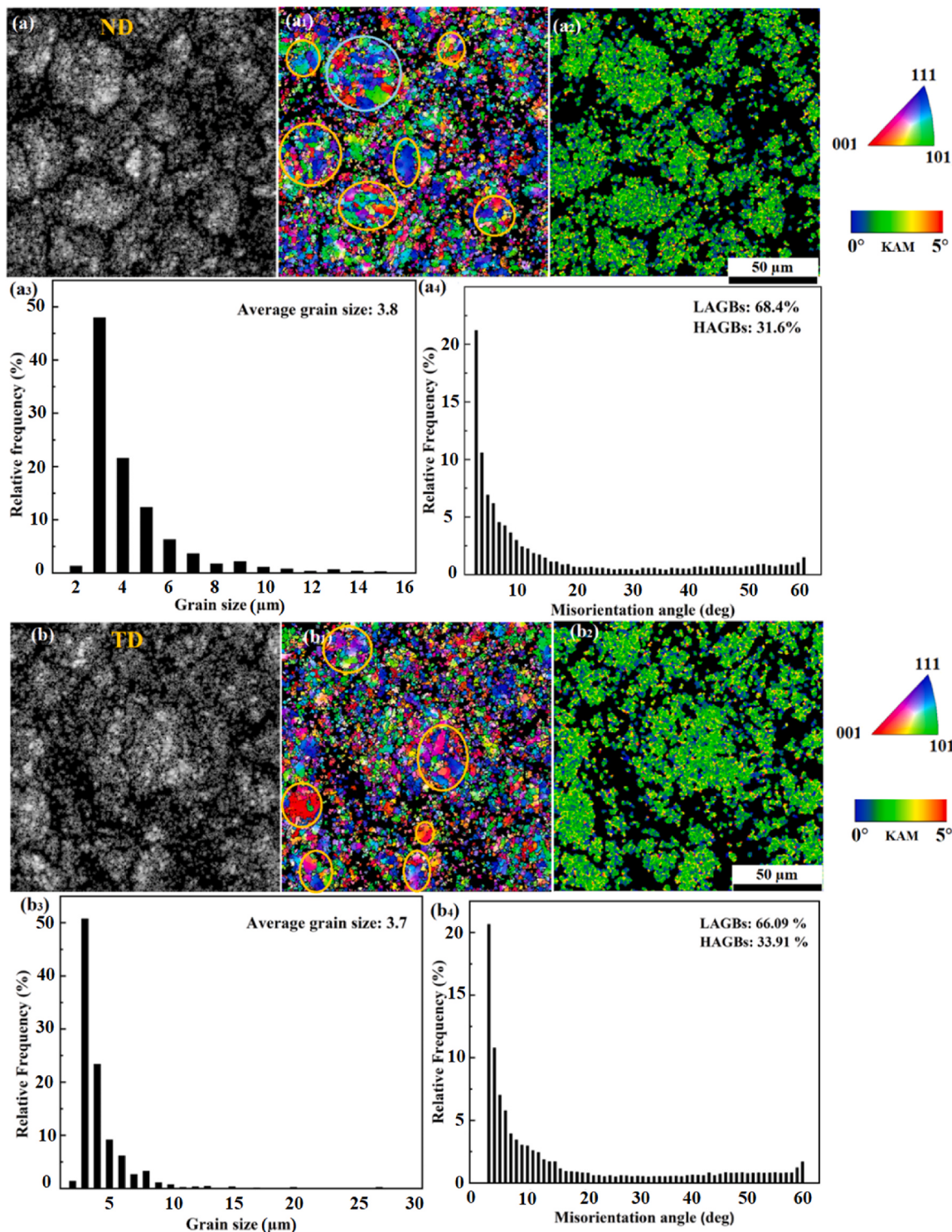
The average grain size and misorientation angle distribution of 1250 °C sintered samples are shown in Fig. 8(d and e). The average grain size of the sintered sample accounted for 73.1 μm (see Fig. 8(d), which is larger than that of the as-sprayed samples (see Fig. 6(b<sub>3</sub>), indicating grain growth. Furthermore, the LAGBs and HAGBs of the sintered HEA were calculated as 15.25 % and 84.75 %, respectively, implying the transformation of ultrafine grains into large equiaxed grains. Also, the sintering twin boundary Σ3 reached 35%, as shown in Fig. 8(e).

Fig. 9 shows the microstructures and corresponding EDS maps of the sintered sample. The results indicate that the distributions of elements such as Co, Cr, Mn, Fe, and Ni are uniform, and each element's atomic and weight percentage is nearly equal after 1250 °C sintering temperature (see Fig. 9(c), and there is no any impurity observed in the sintered sample.

### 3.3. Mechanical properties of the as-sprayed CrCoFeMnNi HEA

The basic mechanical properties of the as-sprayed and sintered vertical and horizontal samples are listed in Table 1. The hardness of the as-sprayed samples is measured to be 376.49 HV, significantly higher than that of other produced CrCoFeMnNi HEA [59,60] due to the severely deformed structure of the as-sprayed deposit. After sintering the as-sprayed sample at 600, 900, and 1100 °C, the hardness was slightly down to 370.6, 362.7, and 350.3 HV, respectively, implying the incomplete recrystallization of the deposit. Then, by increasing the sintering temperatures to 1200 and 1250 °C, the hardness of sintered samples decreased to ~190.90 and 140.92 HV, respectively, implying complete grain growth.

A room-temperature compression test was performed on the as-sprayed and sintered samples. Fig. 10 presents the quasi-static compressive true stress-strain curves for the as-sprayed and sintered vertical and horizontal CoCrFeMnNi HEA samples. The as-sprayed vertical samples had a yield strength (YS) of 1036.6 MPa and ultimate compressive strength (UCS) of 1117.8 MPa at a strain of maximum compressive force of 10.1%. Meanwhile, the as-sprayed horizontal samples of YS 1033.1 MPa and UCS of 1102 MPa were at a strain of 5.6%. However, the as-sprayed sample in both directions shows brittle behavior; the samples immediately failed after reaching UCS, as shown in Fig. 10. Furthermore, the sintered vertical samples had a YS of 266.97



**Fig. 6.** The cold-sprayed CrCoFeMnNi HEA EBSD maps, the first raw displays a horizontal sample, (perpendicular to printing direction, ND), (a) IQ, (a<sub>1</sub>) IPF, (a<sub>2</sub>) KAM, the second raw shows the cold-sprayed horizontal samples histogram (a<sub>3</sub>) grain size distribution (a<sub>4</sub>) local misorientation angle; and the third raw displays, the cold sprayed vertical samples mapping (printing direction, transverse direction, TD), (b) IQ, (b<sub>2</sub>) IPF, and (b<sub>3</sub>) KAM, while the fourth raw shows the cold sprayed vertical samples histogram (b<sub>3</sub>) grain size distribution (b<sub>4</sub>) misorientation angle distribution.

MPa and a UCS of 1048 MPa; no samples failed until the strain reached 70%. Also, the sintered horizontal samples had a YS of 211.9 MPa and UCS of 1009 MPa; no failure occurred until the strain reached 70%. The sintered vertical and horizontal samples did not collapse during the quasi-static test (Fig. 10). Both as-sprayed and sintered vertical samples had higher compressive YS and UCS than the horizontal samples,

implying the anisotropic mechanical behavior.

The as-sprayed samples were brittle under the quasi-static compression test but showed better YS and UCS than the casting methods, as seen in Fig. 10. The reason might be that the as-sprayed samples have numerous finer grains (Fig. 6), which assist the strength by blocking the dislocation motion. Within the same strain rate of 0.001

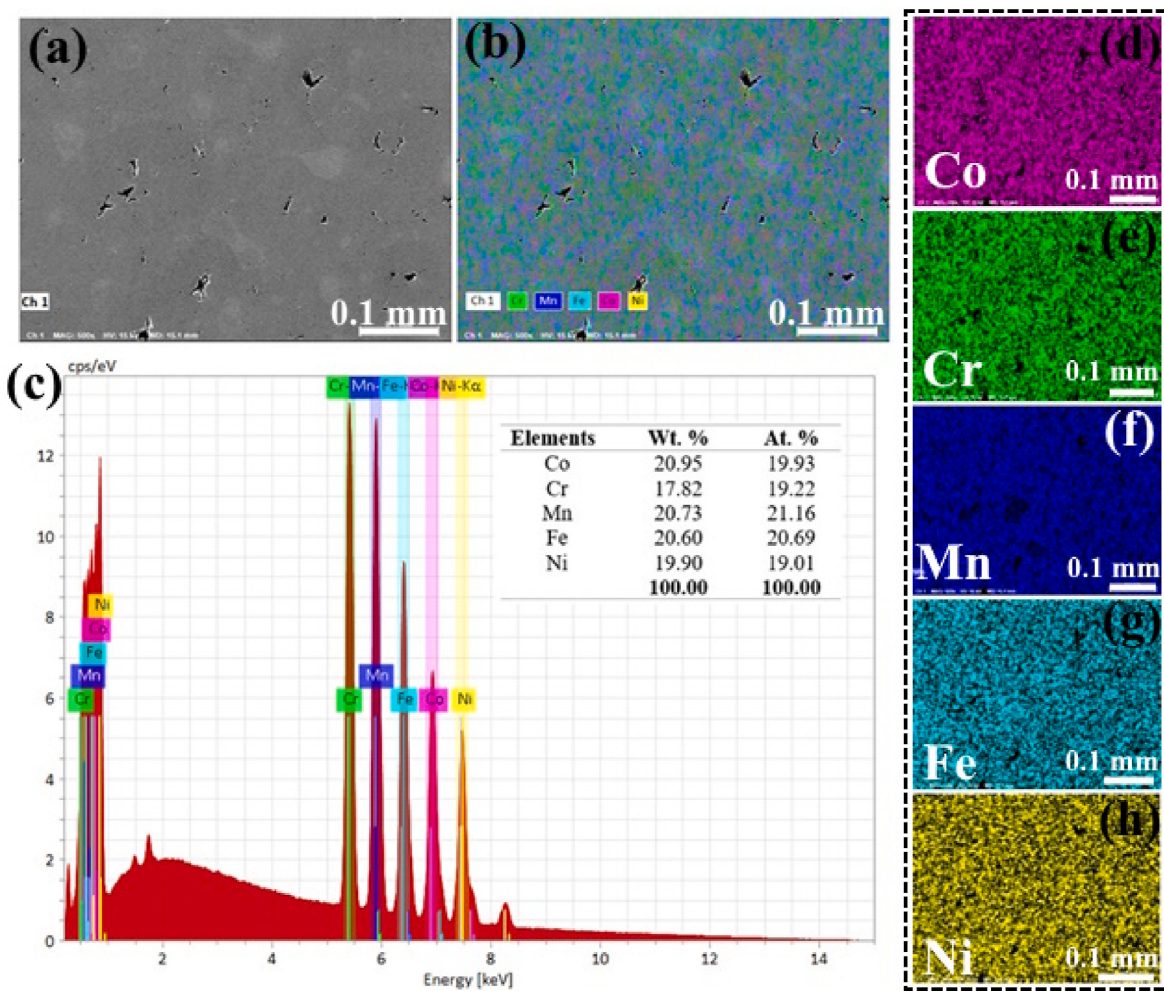


Fig. 7. (a, b), SEM micrographs (c) the EDS spectrum and (d, h) corresponding EDS mapping of the as-sprayed sample.

$s^{-1}$  (Fig. 10), both vertical and horizontal samples showed different YS and UCS, implying an orientation effect and anisotropic properties.

Fig. 11 shows room temperature dynamic compressive true stress-strain curves of the as-sprayed and sintered vertical and horizontal samples performed near the same strain rate. The as-sprayed vertical and horizontal samples showed higher YS and UCS with lower plastic deformation than the sintered samples. The YS and UCS of as-sprayed vertical and horizontal samples at a strain rate of  $3800\text{ s}^{-1}$  were 1068 MPa and 1120 MPa; and 869 MPa and 877 MPa, respectively, which clearly describe the effect of orientation on mechanical properties. The sintered vertical and horizontal samples also exhibited anisotropic behavior due to the different YS and UCS strengths at the same strain rate. Sintered samples showed lower YS and UCS compared to the as-sprayed samples (Fig. 11). The as-sprayed vertical samples under the dynamic test showed higher plastic deformation (Fig. 11), and the sintered samples under the quasi-static test showed excellent ductility, no samples are collapsed (see Fig. 10).

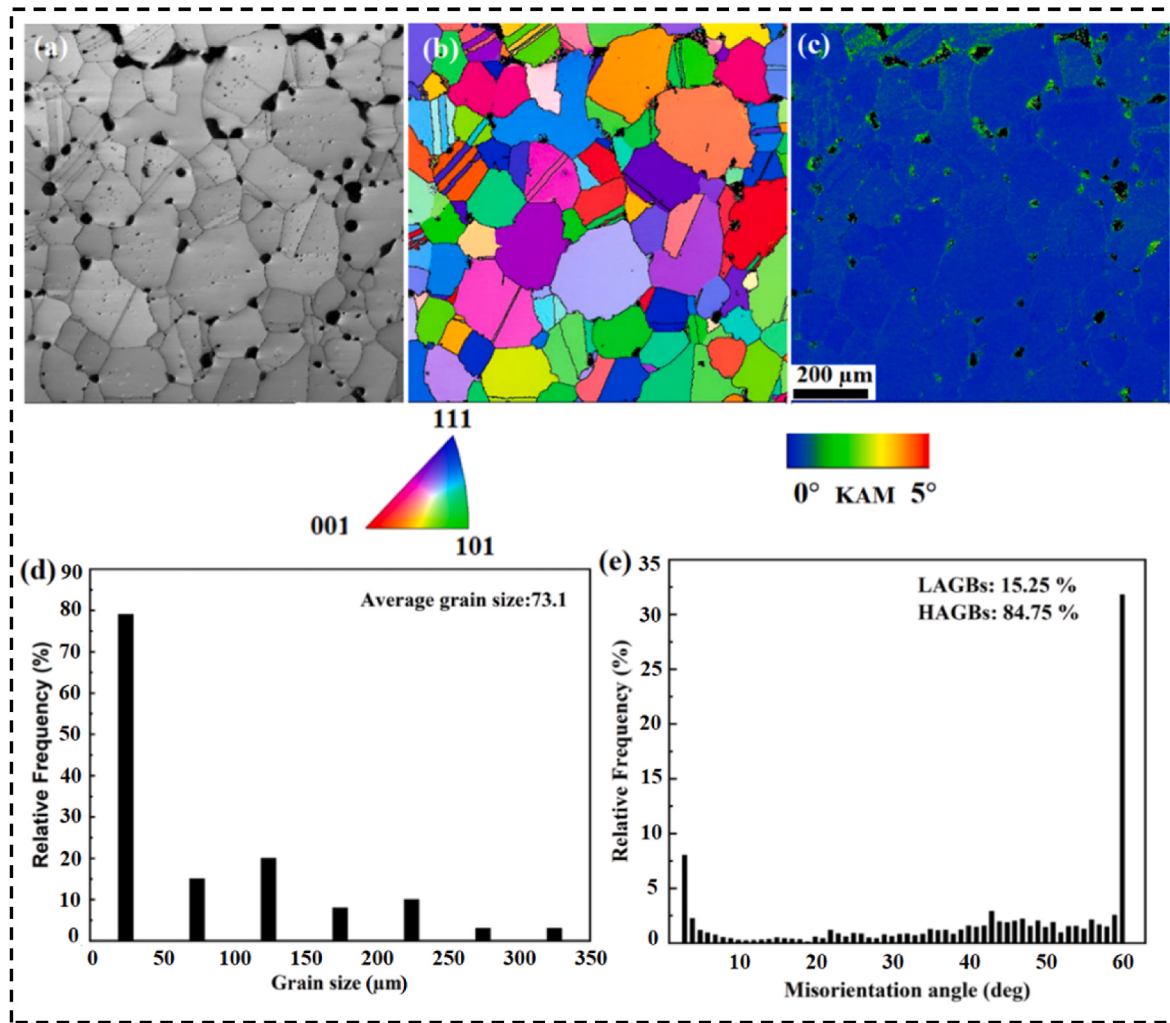
### 3.4. Deformation behavior of as-sprayed and sintered HEA samples

Fig. 13 shows EBSD maps of the deformed as-sprayed vertical CrMnFeCoNi HEA sample under strain rates of  $0.001\text{ s}^{-1}$  at room temperature. EBSD was observed along the Z-direction, the printing and loading direction marked by bright blue arrows in Fig. 13(a). Fig. 13(a) presents the deformed grain structure of the vertical samples under a quasi-static test and exhibits a shear deformation zone marked with white dot lines.

The as-sprayed refined grains shown in Fig. 6(b-b<sub>2</sub>) were completely recrystallized under quasi-static compression (see Fig. 13). It is observed that grains are deformed and developed large shear localization regions, grain refinement, multi-colored elongated grains, and deformation twin indicated by white arrows in Fig. 13(a). The grains indicated by black arrows are DRX grains. Further, DRX grains are revealed in the TEM image in Fig. 14. The KAM map (Fig. 13(b)) shows recrystallization and plastic strain in the shear region. After quasi-static compression, the average grain size (Fig. 13(d)) was highly reduced ( $0.3\text{ }\mu\text{m}$ ) compared to the original as-sprayed sample ( $3.7\text{ }\mu\text{m}$ ) shown in Fig. 6(b<sub>3</sub>). The proportion of LAGBs (Fig. 13(e)) accounts for 55.26%, which is lower than the original as-sprayed sample (66.09%) (Fig. 6(b<sub>4</sub>)) and transformed towards HAGBs due to the applied static load resulting in the plugging of dislocation at grain boundaries.

Fig. 14 shows the TEM microstructure of the vertical sample deformed under quasi-static compression. At the strain rate of  $1 \times 10^{-3}\text{ s}^{-1}$  and room temperature, the as-sprayed samples revealed many deformation twins, dislocation walls, and low stacking faults. The bright field (BF) (Fig. 14(d)) and dark field (DF) images (Fig. 14(g)) indicate a large number of deformation twins in the microstructure. Highly dense dislocation is also observed in HRTEM, which refines the structure. Fig. 14(b) shows the nano-shear band that crosses the twins, where dislocations are formed. DRX grains are observed in the TEM image (Fig. 14(b)), where grains are nucleated in the deformed twins.

Fig. 15 shows the deformed EBSD maps of the sintered vertical CrMnFeCoNi HEA sample under the high strain rate of  $3900\text{ s}^{-1}$  at room temperature. Fig. 15(a) shows the deformed grains structure where the



**Fig. 8.** EBSD map of the sintered ( $1250^{\circ}\text{C}$ ) CrCoFeMnNi HEA with corresponding grain size and misorientation angle distribution histogram, (a) IQ map, (b) IPF map, (c) KAM map, (d) grain size distribution, (e) misorientation angle.

equiaxed grains (Fig. 8(b)) completely disappeared, and large deformed grains appeared. Deformation twins are distributed mainly in the deformed grains shown in Fig. 15(a), indicated by white arrows in which most of the HAGBs (34.8%, see Fig. 15(e)) are concentrated at  $\sim 60^{\circ}$ . In addition, sub-crystalline groups are segregated in the deformed grains with low average orientation difference indicated by yellow arrows in Fig. 15(a). LAGBs (65.2%, see Fig. 15(e)) were concentrated in the deformed region (Fig. 15(c)), which confirms the sub-crystalline groups found in the GBs. It is noted that DRX is one of the deformation mechanisms for high strain rate deformation, as shown in Fig. 15(a), indicated by white dots. It helps to increase grain refinement and random grain orientation. During high strain rates, deformed grains do not have enough time to nucleate and grow; there are continuous regions of original coarse grains.

The grain size ( $2.06\text{ }\mu\text{m}$ ) was very low (Fig. 15(d)) compared to the original sintered sample grain size ( $73.3\text{ }\mu\text{m}$ ) seen in Fig. 8(d). The KAM value (Fig. 15(b)) is higher at DRX, deformation twins, and sub-crystalline grain areas; the higher KAM depicts a significant deformation of grains and higher dislocation density. During the dynamic loading, there is a slight increase in LAGBs fraction, and their concentration is mainly along the GBs of the deformed grains Fig. 15(c). This might be due to the role of the GBs during the DRX process, which may eventually lead to bulging of the GBs (nucleus) before the onset of DRX. Many researchers also reported that the  $\Sigma 3$  twin boundaries are increased during the dynamic loading due to the DRX; the formation of

the  $\Sigma 3$  twin boundaries reduces the boundary energy and facilitates enhanced GB mobility [62].

Fig. 16 shows the TEM microstructure of the sintered vertical sample after dynamic compression test at strain rates of  $3900\text{ s}^{-1}$  and room temperature. After high strain rate deformation, the microstructure is dominated by many deformation twins, dislocations, and low stacking faults. Fig. 16(a and b) shows the grain boundaries, deformation twins, and elongated grains, where the deformation twins interact with grain boundaries. The dark field (Fig. 16(e)) shows a deformation band within the twins' boundaries. Further, cross-linked twins are found in the deformed microstructure, as shown in Fig. 16(e and g). Many parallel deformation twins are observed in BF and DF images (Fig. 16(d and e)). After dynamic compression, nanocrystalline grains are observed, as shown in Fig. 16(c). DRX could form nanocrystals and random grain orientations due to severe plastic deformation.

### 3.5. Fracture analysis of the deformed samples

Fig. 17 presents the fracture morphology of the as-sprayed and sintered HEA under static and dynamic loading. The as-sprayed samples are brittle, and the sintered samples are ductile. Fig. 17(a<sub>1</sub>-a<sub>2</sub>) shows the as-sprayed quasi-static fracture morphology, which exhibits smooth cleavage facets indicating the brittle failure mode. At the same time, Fig. 17(a<sub>3</sub>) presents the sintered vertical samples static compression fracture morphology showing irregular & fibrous structure, spherical

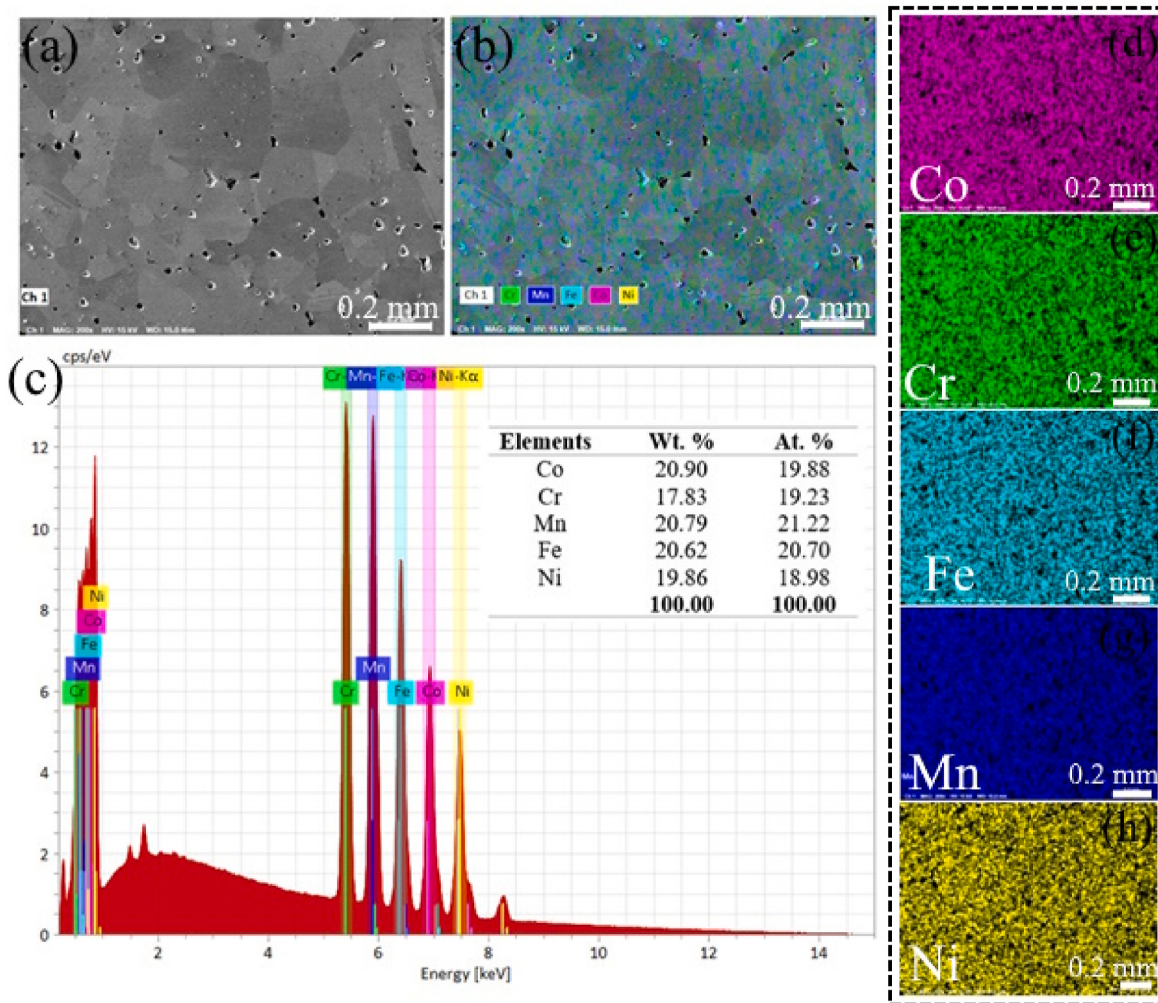


Fig. 9. (a, b), SEM micrographs (c) the EDS spectrum, and (d, h) corresponding EDS mapping of the sintered sample.

**Table 1**  
Basic properties of the as-sprayed and sintered samples.

Sample property	As-sprayed	600 °C/1h	900 °C/1h	1100 °C/1h	1200 °C/1h	1250 °C/1h
Density (g/cm <sup>3</sup> )	7.57 ± 0.003	7.58 ± 0.001	7.67 ± 0.002	7.68 ± 0.003	7.73 ± 0.002	7.77 ± 0.01
Rel. Density (%)	95	95	96	96.4	97	97.5
Fraction porosity (%)	11 ± 0.4	10.8 ± 0.1	10.01 ± 0.2	8.05 ± 0.03	5 ± 0.3	4 ± 0.2
Hardness (HV)	376.49	370.6	362.7	350.3	190.90	140.92

dimples, and microcavities observed in fracture surface indicative of plastic deformation and ductile fracture mode. The fracture surface of the as-sprayed sample (Fig. 17(a<sub>1</sub>-a<sub>2</sub>)) displays the different orientations of cleavage planes, and cracks are propagated along grain boundaries. For the dynamic loading at a strain rate of 3900 s<sup>-1</sup> the fracture mode is a *trans-granular* cleavage facet, in which high-density deformation was observed in as-sprayed and sintered samples (seen in Fig. 17(b<sub>1</sub>-b<sub>3</sub>)). The fractography features of vertical and horizontal samples were quite different.

#### 4. Discussion

The as-sprayed vertical and horizontal samples exhibit extraordinary mechanical properties, especially the YS and UCS, compared to any manufacturing methods for this alloy. The as-sprayed vertical samples had a YS of 1036.6 MPa and UCS of 1117.8 MPa at a strain elongation of

10.1% under a strain rate of 0.001 s<sup>-1</sup>. The as-sprayed horizontal samples had a YS of 1033.1 MPa and a UCS of 1102 MPa at a strain elongation of 5.6% under a strain rate of 0.001 s<sup>-1</sup>. Furthermore, the YS and UCS of as-sprayed vertical and horizontal samples at a strain rate of 3800 s<sup>-1</sup> were 455 MPa and 497 MPa and 356 MPa and 387 MPa, respectively. Also, the sintered vertical and horizontal samples showed significantly higher in YS and UCS than the cast CrCoFeMnNi HEA [61, 62], as presented in Fig. 12. Thus, the mechanical performance of as-sprayed deposits is expected to be suitable for structural application.

##### 4.1. The strengthening mechanisms

The strengthening mechanisms of as-sprayed CoCrFeMnNi HEA will be discussed. The contributing factors for the higher YS of the as-sprayed samples are the summation of individual strengthening mechanisms, such as (i) grain refinement strengthening ( $\sigma_g$ ), (ii) residual dislocation

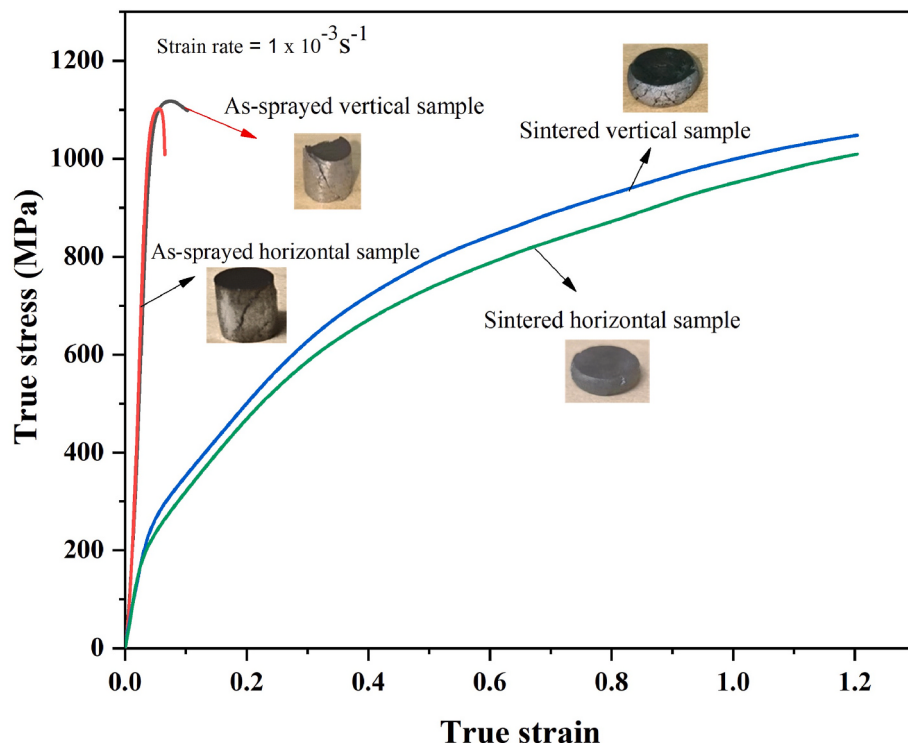


Fig. 10. Quasi-static compression true stress-strain curve for as-sprayed and sintered HEA samples at room temperature and strain rate of  $1 \times 10^{-3} \text{ s}^{-1}$ .

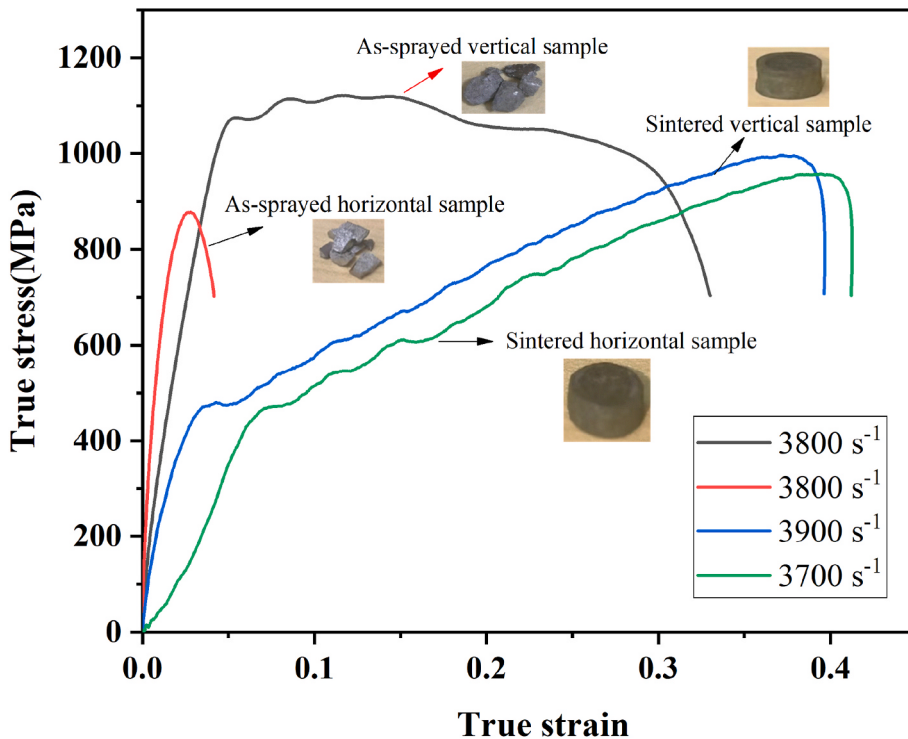


Fig. 11. Dynamic compression true stress-strain curve for as-sprayed and sintered HEA samples at room temperature and different strain rates.

density ( $\sigma_d$ ), (iii) solid solution strengthening ( $\sigma_{ss}$ ), (iv) lattice friction stress ( $\sigma_{fr}$ ), and (V) precipitation strengthening ( $\sigma_{ppt}$ ). No precipitates were observed from TEM analysis (Figs. 14 and 16), so we neglect the  $\sigma_{ppt}$  contribution. For the  $\sigma_{fr}$  strengthening contribution, we used 154 MPa, reported in Ref. [63]. Therefore, the yield strength  $\sigma_{(0.2)}$  can be computed:

$$\sigma_{(0.2)} = \sigma_{fr} + \sigma_{ss} + \sigma_d + \sigma_g \quad (7)$$

#### 4.1.1. Grain refinement strengthening

The EBSD map (Fig. 6) of the sprayed horizontal and vertical samples revealed refined grains with average grain sizes of 3.8  $\mu\text{m}$  and 3.7  $\mu\text{m}$ , respectively. Also, after quasi-static deformation, the as-sprayed sample

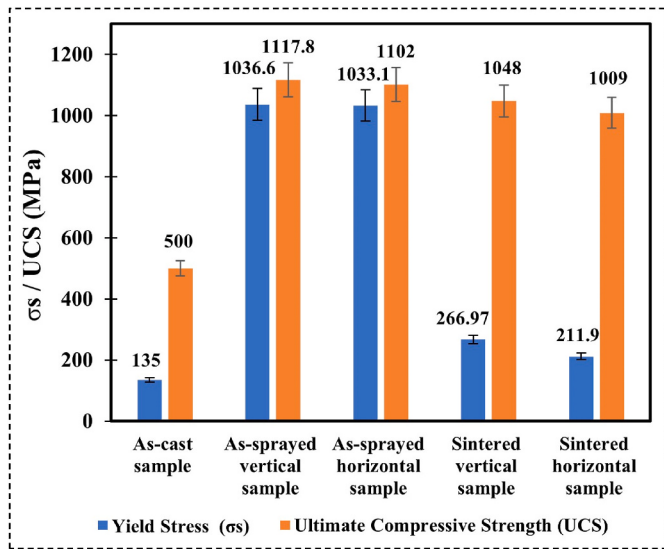


Fig. 12. Comparison of the as-cast sample (average) [61,62] and as-sprayed quasi-static yield strength ( $\sigma_s$ ) and ultimate compressive strength (UCS) of the present study.

microstructure showed large refined DRX grains along the sheared area (Fig. 13) with a grain size of 0.3  $\mu\text{m}$ . Similarly, after dynamic compression, the sintered samples (Fig. 15) showed a significant level of DRX grains in the deformed region with a grain size of 2.06  $\mu\text{m}$ . Thus, the deformed as-sprayed (Fig. 13(d)) and sintered sample (Fig. 15(d)) showed grain refinement due to DRX [64]. Also, several deformation twins are observed in EBSD (Figs. 13(a), and Fig. 15(a)) as well as in TEM (Figs. 14, and Fig. 16), which are essential to hinder dislocation motion and provide a greater driving force for the nucleation and growth of DRX grains [65]. It is well known that grain refinement is a known factor for the hardening of materials, especially during deformation governed by the Hall–Petch effect [66];

$$\sigma_Y(d) = \sigma_0 + k_y^{HP} d^{-\frac{1}{2}} \quad (8)$$

$$\sigma_g = \frac{k_y^{HP}}{\sqrt{d}} \quad (9)$$

where  $\sigma_Y(d)$  is the yield strength due to the reduced grain size,  $\sigma_0$  is the intrinsic yield strength for large grains,  $d$  is average grain diameter, and  $k_y^{HP}$  is the Hall-Petch coefficient. The  $k_y^{HP}$  of CoCrFeMnNi HEA is 490 MPa  $\mu\text{m}^{-0.5}$  [67,68], and from our experiment, the average grain size of the as-sprayed sample is ( $d = 3.7 \mu\text{m}$ ), then, using Eq. (9) the strength increments due to  $\sigma_g$  is 255 MPa. Also, the  $\sigma_g$  of sintered sample ( $d = 73.1 \mu\text{m}$ ) was obtained as 58 MPa.

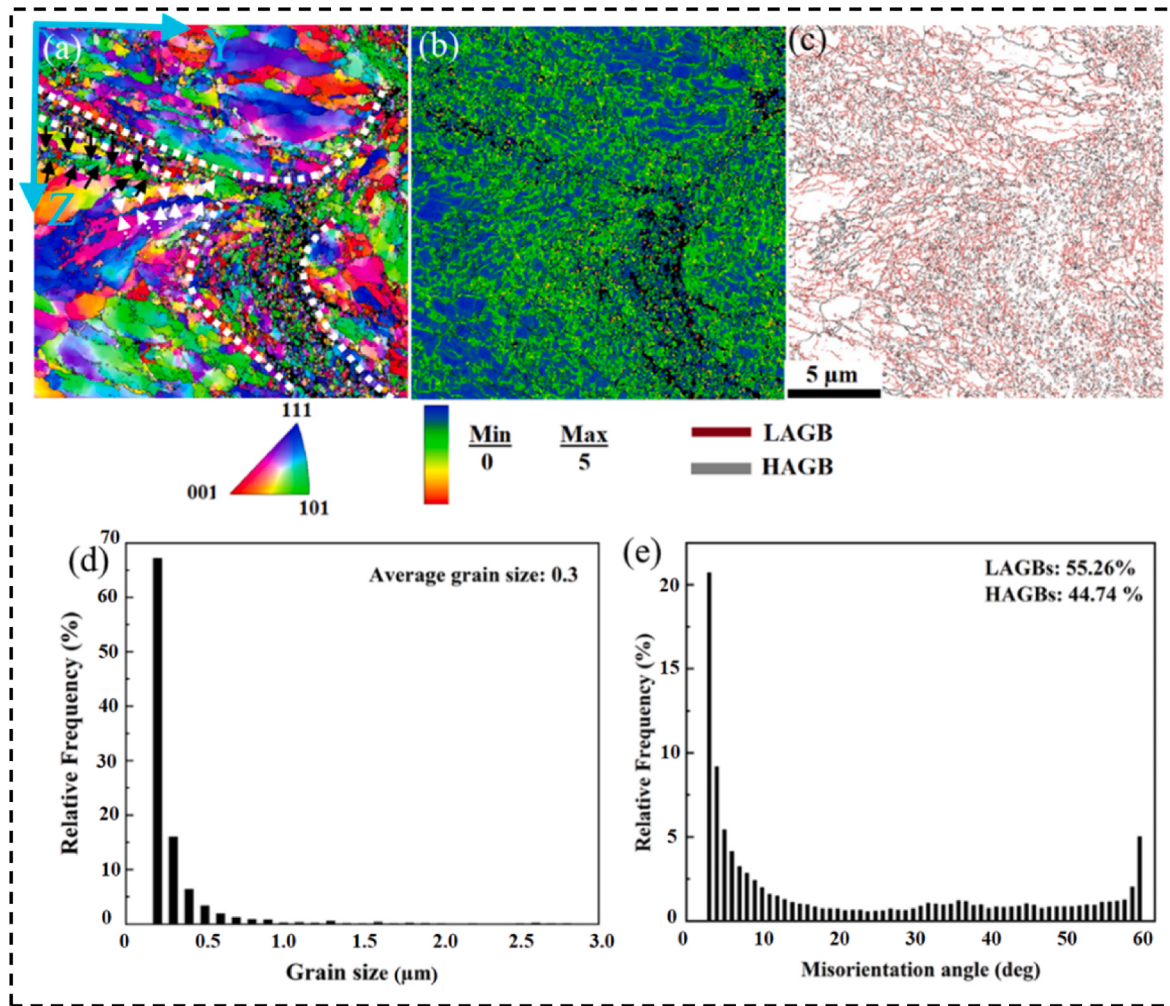
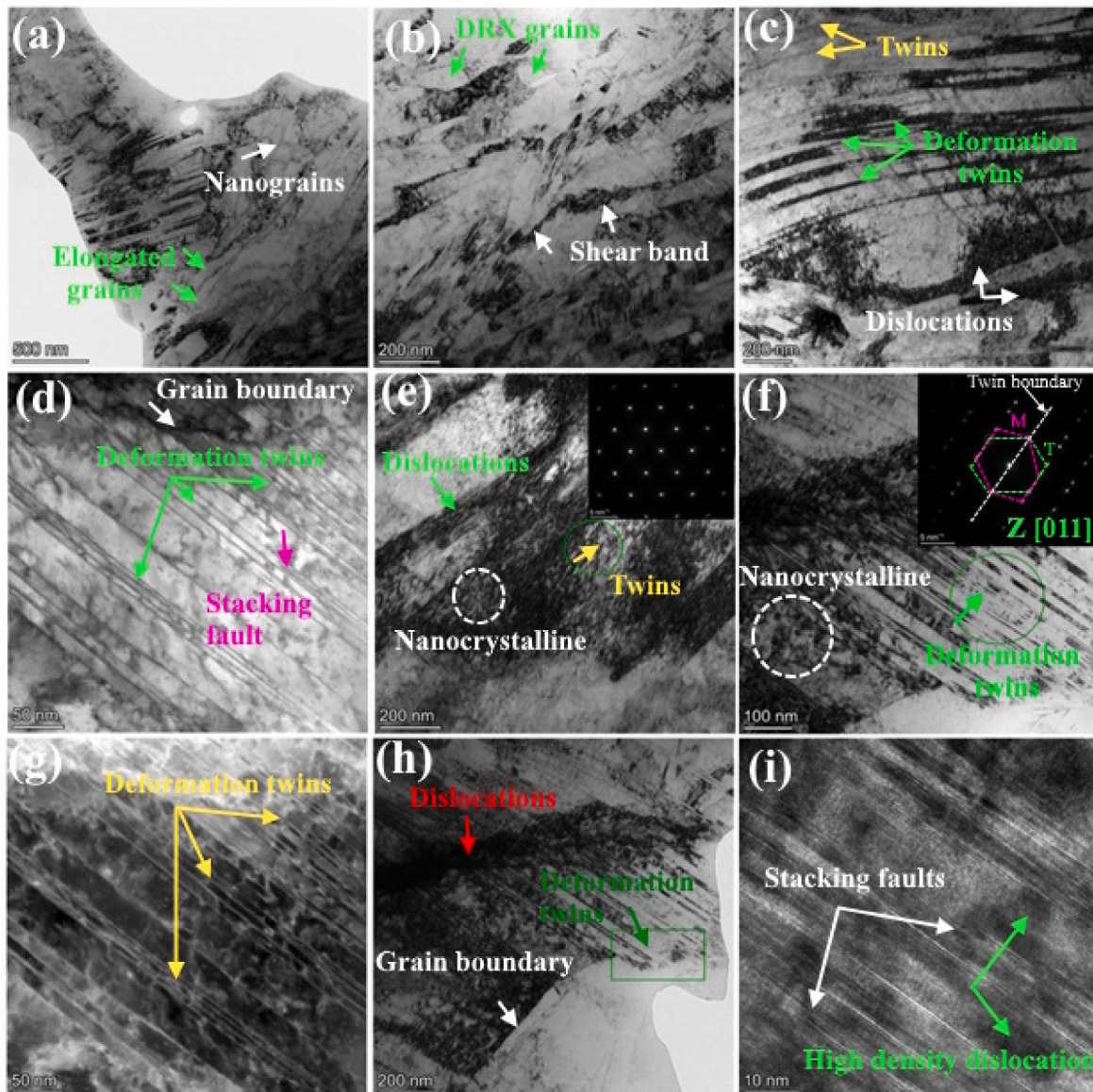


Fig. 13. EBSD maps for compressive deformation of the as-sprayed vertical sample under strain rates of  $0.001 \text{ s}^{-1}$  (a) grain structure, (b) KAM, (c) grain boundary, (d) grain size distribution, (e) misorientation angle distribution.



**Fig. 14.** TEM micrograph and corresponding SAED patterns of the as-sprayed vertical sample compression test under strain rates of  $0.001 \text{ s}^{-1}$ : (d) BF image, (g) DF image, and (i) HRTEM image.

#### 4.1.2. Residual dislocation strengthening

A large amount of dislocation density occurred during the CS due to the plastic deformation of particles, which could play an essential role in the hardening of the material. Figs. 13(c) and 15(c) show a high concentration of low-angle grain boundaries, about 55.26%, and 65.2%, respectively, indicating the formation of geometrically necessary dislocation density. To estimate the residual dislocation yield strength increment using the Taylor formula [69]:

$$\sigma_d = \alpha M G b \rho^{\frac{1}{2}} \quad (10)$$

where  $\alpha = 0.2$  is constant for FCC materials,  $M = 3.06$  is Taylor factor, Shear modulus ( $G$ ) = 80 GPa from Ref. [70],  $b$  is Burger's vector, and  $\rho$  is dislocation density in the sample. The dislocation density ( $\rho$ ) of the cold-sprayed deposit was calculated from the crystallite diameter ( $d$ ) and microstrain ( $\epsilon$ ) [66],

$$\rho = \frac{2\sqrt{3}\epsilon}{db} \quad (11)$$

where  $b$  is the Burgers vector  $b = \frac{\sqrt{2}}{2}a$  for fcc metals,  $a = 3.6 \text{ \AA}$  is the lattice parameter; then,  $b = 2.5 \text{ nm}$ . The crystallite diameters and estimated residual strain of the feedstock powders, as-sprayed, and sintered samples were calculated by Eq. (6) as discussed in section 3.1. The cold-sprayed deposit showed higher dislocation density than the feedstock powder and sintered samples, indicating that a large dislocation occurred during CS fabrication, then a yield strength increment of the as-sprayed sample is  $\sigma_d = 180 \text{ MPa}$ , while the dislocation density ( $\rho$ ) of the as-sprayed sample =  $1.1 \times 10^{10} \text{ m}^{-2}$  computed from XRD diffraction. However, the results may vary with other measuring techniques, because X-ray diffraction measures the coherent diffraction domains, including dislocation cells and subgrains [56].

#### 4.1.3. Solid solution strengthening

The XRD pattern (Fig. 4) confirms a single-phase FCC solid solution with a lattice parameter of  $3.6 \text{ \AA}$ . In addition, the as-sprayed (Fig. 7) and sintered sample (Fig. 9) revealed an equal concentration of elements 19.93 at% of Co, 19.22 at% of Cr, 21.16 at% of Mn, 20.69 at% of Fe, and 19.01 at% of Ni as observed from EDS of TEM which confirms robust

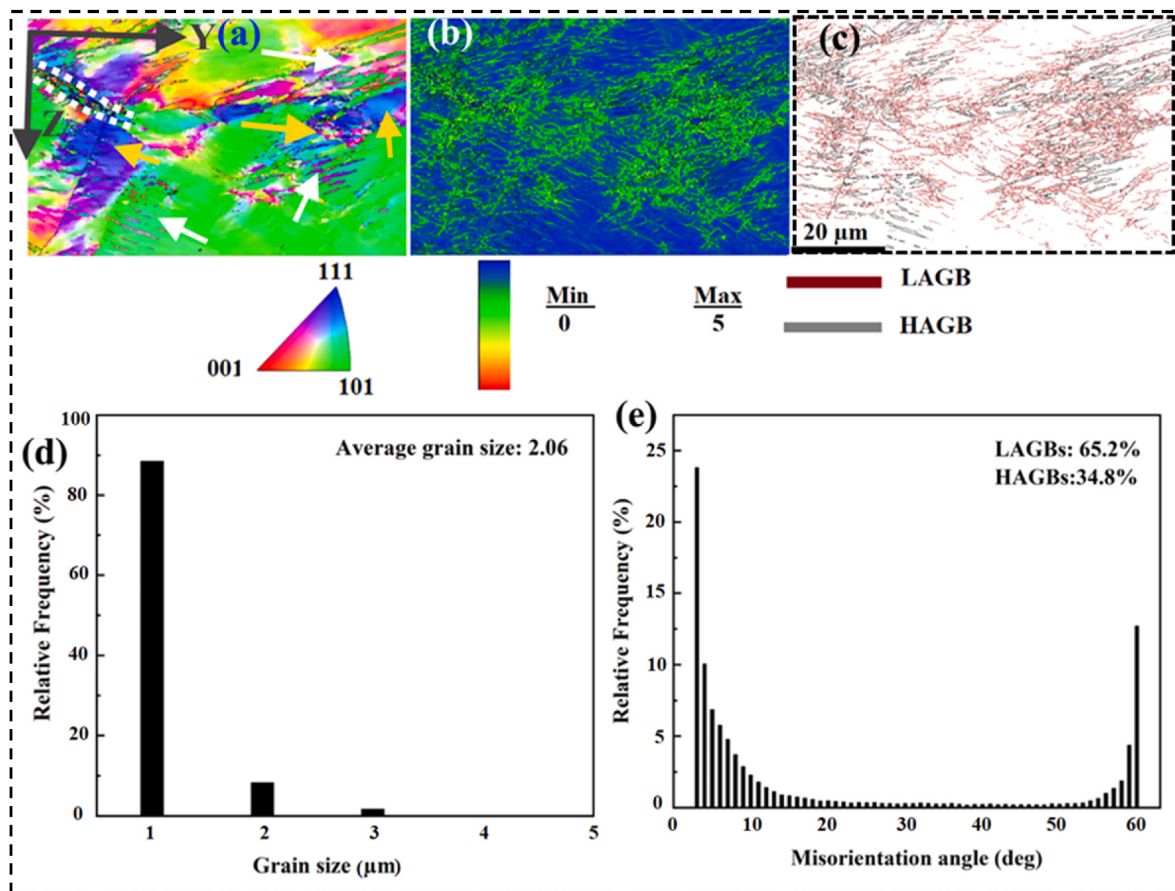


**Fig. 15.** EBSD maps of the sintered vertical sample under dynamic ( $3900\text{ s}^{-1}$ ) compression test.

solid solution softening effect. The solid solution strengthening ( $\sigma_{ss}$ ) can be quantified by  $\sigma_{ss} = \sigma_Y - \sigma_{fr} - \sigma_d - \sigma_g$ , which is about 448 MPa, implying the highest strengthening contribution compared to other mechanisms.

Therefore, from the above analysis, the yield strength of the as-sprayed sample is the sum of grain refinement ( $\sigma_g = 255\text{ MPa}$ ), residual dislocation density ( $\sigma_d = 180\text{ MPa}$ ), solid solution strengthening ( $\sigma_{ss} = 448\text{ MPa}$ ), lattice friction stress ( $\sigma_{fr} = 154\text{ MPa}$ ), it should consistent with the experimental value,  $\sigma_Y \sim 1036.6\text{ MPa}$ .

#### 4.2. Effect of sintering on mechanical properties

**Fig. 5(a)** and **Fig. 6** show the microstructure of the as-fabricated sample exhibiting residual stress, undeformed particles, fine and elongated grains, and interparticle pores. Those have appreciable and/or depreciable effects on the mechanical properties of the as-fabricated sample. The as-sprayed HEA samples showed brittle behavior during the quasi-static and dynamic compression test. However, sintering improved the inter-particle bonding and relieved the stored stress. Sintering activates grain migration via recovery, recrystallization, and grain growth to make the materials ductile [52,71]. At  $1250^\circ\text{C}$  sintering temperature, the numerous refined grains, micropores, and elongated grains of the as-sprayed samples shown in **Fig. 5(a)**, and **Fig. 6** are recrystallized into large equiaxed grains and spherical pores as seen in **Fig. 8**. Micropores and large pores are formed at grains and grain boundaries respectively [52]. As listed in **Table 1**, the densities of the as-sprayed sample increased from  $7.57\text{ g/cm}^3$  to  $7.77\text{ g/cm}^3$  as the sintering temperature increased from  $600$  to  $1250^\circ\text{C}$ .

The sintered samples (**Figs. 10 and 11**) exhibit lower yield and ultimate compressive strength than as-fabricated samples. The  $1250^\circ\text{C}$  sintered sample showed higher mechanical plasticity. However, the YS

dramatically decreases due to the reduction of dislocations. As shown in **Fig. 8**, the grains are growing into large grains, and as the grain's size increases, dislocations are significantly decreased, and finally, the YS is reduced. It is well known that high-temperature sintering causes structural ductility. The as-sprayed and sintered samples remain a single fcc structure (**Fig. 4**), and the ductility is mainly caused by grain growth. The measured value of hardness (**Table 1**) was used to represent the yield strength of as-sprayed and sintered sample deposits as a function of grain size using the classical Hall–Petch relationship [72]:

$$H = H_0 + k_{hp} d^{-1/2} \quad (12)$$

where  $H_0$  is the intrinsic hardness of the deposit,  $d$  is the average grain size, and  $k_{hp}$  is the Hall–Petch coefficient. The value of  $k_{hp}$  for the FeCoNiCrMn HEA is  $677\text{ MPa }\mu\text{m}^{-0.5}$  from Ref. [72]. Using Eq. (12), the  $\sigma_Y$  of the as-sprayed as a function of grain size ( $d = 3.7\text{ }\mu\text{m}$ ) is  $1302\text{ MPa}$ , and the  $\sigma_Y$  of the sintered sample ( $d = 73.1$ ) is  $237\text{ MPa}$ ; however, due to the higher porosity in the as-sprayed sample, the results somehow deviated from experimental values. In addition, several researchers reported [73,74] the relationship between hardness ( $H_v$ ), and yield strength ( $\sigma_Y$ ) is computed by:

$$H_v = 3\sigma_Y \quad (13)$$

Using Eq. (13), the yield strength of as-sprayed and sintered samples are approximately equal to the experimental values of this work.

#### 4.3. Effect of printing direction on mechanical properties

The experimental results of cold-sprayed CrCoFeMnNi HEA showed anisotropic mechanical properties (as seen in **Figs. 10**, **Fig. 11**, and **Fig. 12**). However, we did not observe apparent anisotropic

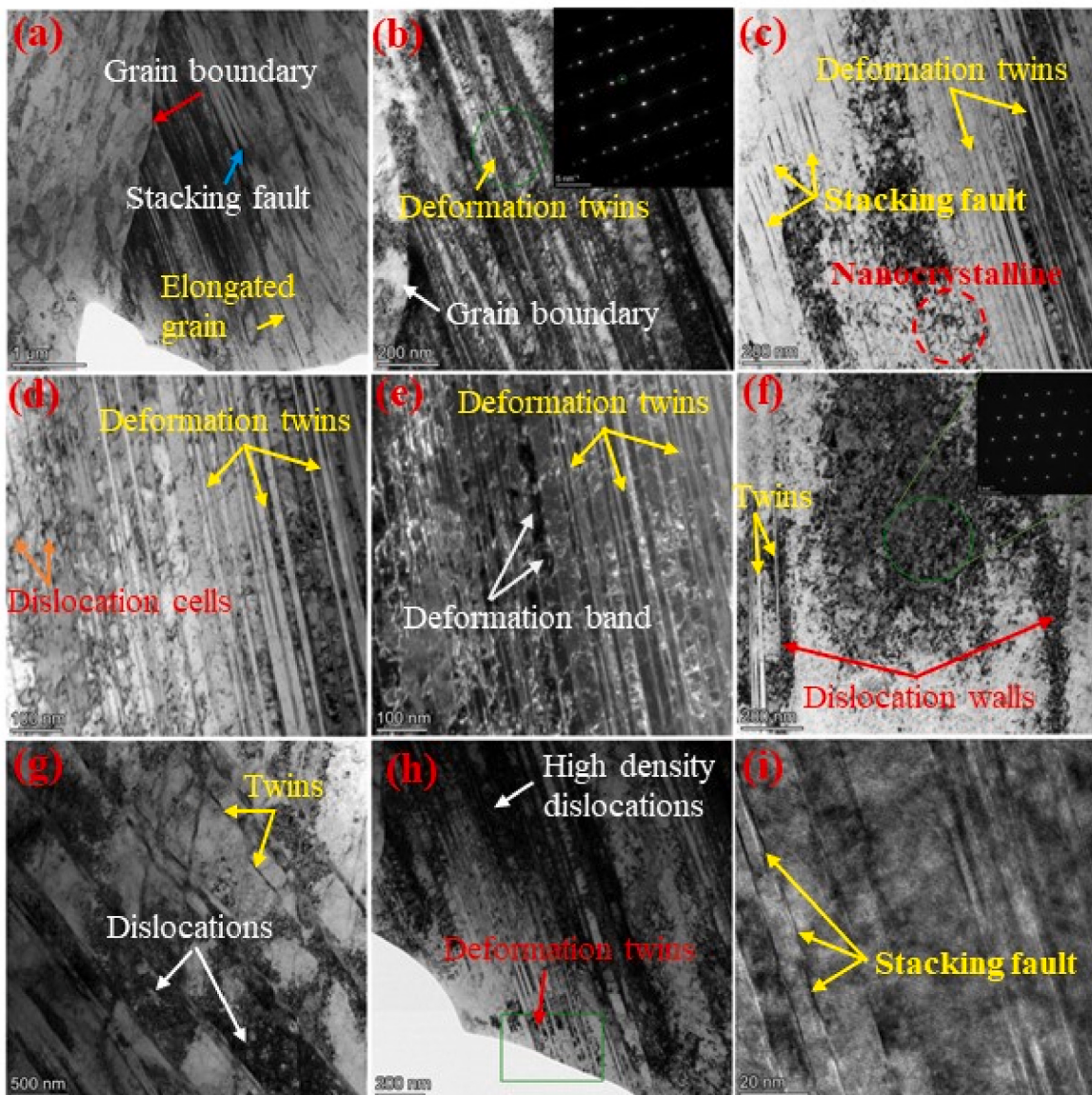


**Fig. 16.** TEM micrograph and corresponding SAED patterns of the sintered vertical sample compression test under strain rates of  $3900\text{ s}^{-1}$ : (a–d) BF image, (e) DF image, (f–h) BF image, and (i) HRTEM image.

microstructure in Fig. 6. The anisotropic behavior of CSAM was observed and reported by many researchers [75–77]; in most of these researches, the microstructure in the printing direction and perpendicular to it is different. To examine the effect of printing direction on the mechanical properties of cold-sprayed CrCoFeMnNi HEA deposit, we have performed the quasi-static and dynamic compressive test (as seen in Figs. 10 and 11, respectively) of as-fabricated and sintered vertical and horizontal samples at similar strain rate. The horizontal sample had lower YS and UCS than vertical samples due to inter-particle boundaries and microporosity developed in the cross-sectional surface than in the printing direction. The inhomogeneous particle impact deformation and the different inter-particle interface behavior during CS might result in mechanical anisotropies. Another reason for the difference in mechanical properties between horizontal and vertical samples was the different fracture modes (see Fig. 17); fractography of the broken samples showed different fracture modes for horizontal and vertical samples. Moreover, few dimples occurred in the horizontal samples. Fig. 6(a and b) displays the distorted crystal lattice owing to a high concentration of strain appearing in darker regions, and numerous refined grains are observed

in Fig. 6(a<sub>1</sub>, b<sub>1</sub>), implying that the more particles deformation and recrystallization [76,77]. In addition, the presence of refined grains and higher inter-particle bonding in the vertical samples helps as a blocking mechanism for compressive dislocation motion, resulting in higher YS and UCS.

## 5. Conclusion

This study investigated the compressive behavior of cold-sprayed bulk CrCoFeMnNi HEA. The equiautomic CrCoFeMnNi HEA powder was cold sprayed on Al6061 substrate using nitrogen as processing gas at a particle temperature of  $600\text{ }^\circ\text{C}$  and pressure of 4.2 MPa. The quasi-static and dynamic compressive tests were conducted at room temperature to examine the deformation behavior of the as-sprayed deposit. Based on the findings, the following conclusion can be drawn:

- The as-fabricated samples exhibit undeformed particles, fine and elongated grains, and interparticle pores, resulting in the brittle behavior of the as-sprayed sample.

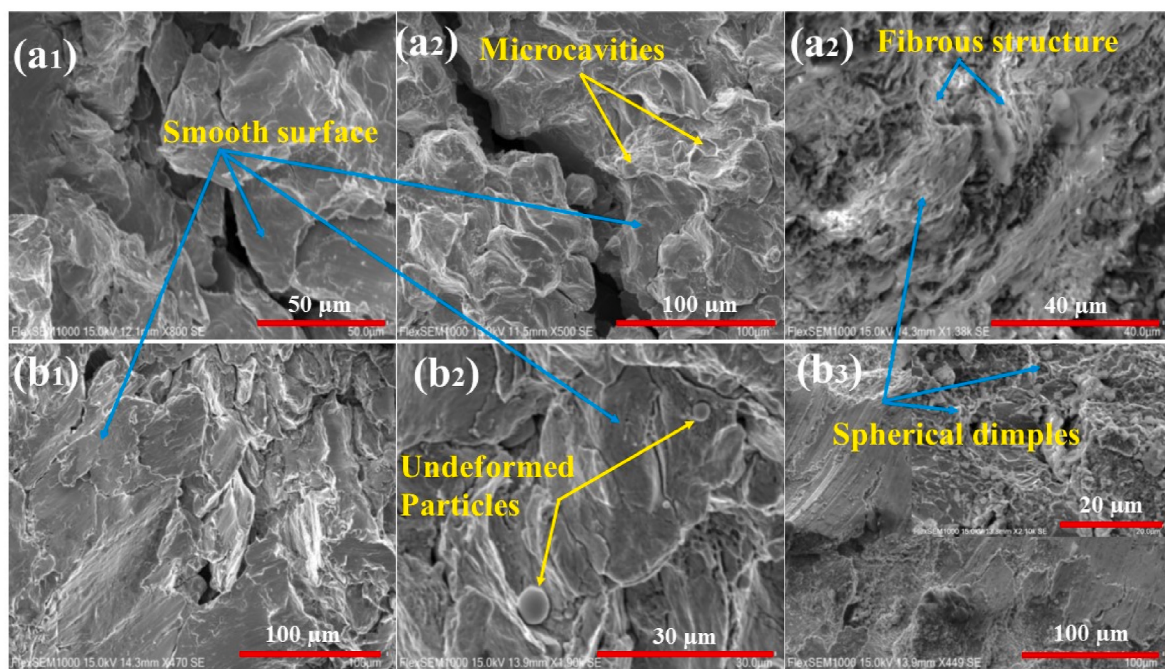


**Fig. 17.** The fracture morphology of the as-sprayed and sintered HEA under different strain rates: (a<sub>1</sub>-a<sub>3</sub>) at a strain rate of 0.001 s<sup>-1</sup> and (b<sub>1</sub>-b<sub>2</sub>) at a strain rate of 3800 s<sup>-1</sup>, and (b<sub>3</sub>) 3900 s<sup>-1</sup> respectively. (a<sub>1</sub>, b<sub>1</sub>) as-sprayed vertical, (a<sub>2</sub>, b<sub>2</sub>) as-sprayed horizontal, (a<sub>3</sub>) sintered vertical sample, and (b<sub>3</sub>) sintered horizontal sample.

- The as-sprayed deposit shows outstanding mechanical compressive strength. The as-sprayed vertical samples had a YS of 1036.6 MPa and UCS of 1117.8 MPa at a strain elongation of 10.1%. Also, the as-sprayed horizontal samples had a YS of 1033.1 MPa and a UCS of 1102 MPa at a strain elongation of 5.6%.
- The average microhardness of the as-sprayed sample was measured to be  $3.6 \pm 0.2$  GPa, which is higher than that of conventional casting. The as-sprayed samples' porosity was  $11 \pm 0.4$  %, with a porosity of  $4 \pm 0.2$  %, whereas the sintered samples exhibited a sharp hardness decrease to  $1.35 \pm 0.2$  GPa.
- The dominant deformation mechanism of this work was deformation twinning.

This paper showed outstanding yield and ultimate compressive strength compared to other CrCoFeMnNi HEA manufacturing methods. The optimum post-heat treatment process improves the unfavorable mechanical properties of the CSAM deposits.

#### CRediT authorship contribution statement

**Bemechal Tsegaye Mengiste:** Writing – review & editing, Writing – original draft, Visualization, Validation, Software, Methodology, Investigation, Formal analysis, Data curation, Conceptualization. **Ali Arab:** Writing – review & editing, Writing – original draft, Validation, Supervision, Methodology, Investigation, Data curation, Conceptualization. **Yansong Guo:** Visualization, Formal analysis. **Yinze Lei:** Visualization, Formal analysis. **Xiaoshuai Li:** Visualization, Formal analysis. **Pengwan Chen:** Resources, Project administration, Funding acquisition. **Jing Xie:** Writing – review & editing, Supervision, Resources, Project administration, Funding acquisition.

#### Declaration of competing interest

The authors declare that they have no known competing financial interests or personal relationships that could have appeared to influence the work reported in this paper.

#### Data availability

Data will be made available on request.

#### Acknowledgments

The authors are grateful for the financial support from the National Nature Science Foundation of China (NSFC, No. 12002052, No. 12272053 and No. 12072038).

#### References

- [1] B. Cantor, Multicomponent high-entropy Cantor alloys, *Prog. Mater. Sci.* 120 (2021) 100754, <https://doi.org/10.1016/j.pmatsci.2020.100754>.
- [2] J.W. Yeh, Alloy design strategies and future trends in high-entropy alloys, *Jom* 65 (2013) 1759–1771, <https://doi.org/10.1007/s11837-013-0761-6>.
- [3] E.P. George, W.A. Curtin, C.C. Tasan, High entropy alloys: a focused review of mechanical properties and deformation mechanisms, *Acta Mater.* 188 (2020) 435–474, <https://doi.org/10.1016/j.actamat.2019.12.015>.
- [4] A. Arab, Y. Guo, Z. Dilshad Ibrahim Sktni, P. Chen, Effect of strain rate and temperature on deformation and recrystallization behaviour of BCC structure AlCoCrFeNi high entropy alloy, *Intermetallics* 147 (2022) 107601, <https://doi.org/10.1016/j.intermet.2022.107601>.
- [5] B. Cantor, Multicomponent high-entropy Cantor alloys, *Prog. Mater. Sci.* 120 (2021) 100754, <https://doi.org/10.1016/j.pmatsci.2020.100754>.
- [6] B. Cantor, I.T.H. Chang, P. Knight, A.J.B. Vincent, Microstructural development in equiatomic multicomponent alloys, *Mater. Sci. Eng. A* 375–377 (2004) 213–218, <https://doi.org/10.1016/j.msea.2003.10.257>.
- [7] S.Y. Ahn, D.G. Kim, J.A. Lee, E.S. Kim, S.G. Jeong, R.E. Kim, J. Choe, S.J. Hong, P. Quang, S. Lee, H.S. Kim, Dynamic compression behavior of CoCrFeMnNi high-entropy alloy fabricated by direct energy deposition additive manufacturing, *J. Alloys Compd.* 960 (2023) 170602, <https://doi.org/10.1016/j.jallcom.2023.170602>.
- [8] S. Xiang, H. Luan, J. Wu, K. Yao, J. Li, X. Liu, Microstructures and mechanical properties of CrMnFeCoNi high entropy alloys fabricated using laser metal deposition technique, *J. Alloys Compd.* 773 (2019) 387–392, <https://doi.org/10.1016/j.jallcom.2018.09.235>.
- [9] Y.K. Kim, J. Choe, K.A. Lee, Selective laser melted equiatomic CoCrFeMnNi high-entropy alloy: microstructure, anisotropic mechanical response, and multiple strengthening mechanism, *J. Alloys Compd.* 805 (2019) 680–691, <https://doi.org/10.1016/j.jallcom.2019.07.106>.
- [10] M. Jin, E. Hosseini, S.R. Holdsworth, M. Pham, Thermally activated dependence of fatigue behaviour of CrMnFeCoNi high entropy alloy fabricated by laser powder-bed fusion, *Addit. Manuf.* 51 (2022) 102600, <https://doi.org/10.1016/j.addma.2022.102600>.

- [11] Y. Kim, K. Lee, Journal of Materials Science & Technology ultra-strong CrMnFeCoNi high-entropy alloy additively manufactured by laser powder bed fusion, *J. Mater. Sci. Technol.* 117 (2022) 8–22, <https://doi.org/10.1016/j.jmst.2021.12.010>.
- [12] C. Wang, Y. Yu, J. Yu, Y. Zhang, F. Wang, Effect of the macro-segregation on corrosion behavior of CrMnFeCoNi coating prepared by arc cladding, *J. Alloys Compd.* 846 (2020) 156263, <https://doi.org/10.1016/j.jallcom.2020.156263>.
- [13] S. Feng, S. Guan, W.A. Story, J. Ren, S. Zhang, A. Te, M.A. Gleason, J. Heelan, C. Walde, A. Birt, K.L. Tsaknopoulos, D.L. Cote, W. Kapalcynski, A.T. Naardi, V. K. Champagne, M.J. Siopis, W. Chen, Cold spray additive manufacturing of CoCrFeNiMn high-entropy alloy: process development, microstructure, and mechanical properties, *J. Therm. Spray Technol.* 31 (2022) 1222–1231, <https://doi.org/10.1007/s11666-022-01374-4>.
- [14] R. Nikbakht, M. Saadati, T.S. Kim, M. Jahazi, H.S. Kim, B. Jodoin, Cold spray deposition characteristics and bonding of CrMnCoFeNi high entropy alloy, *Surf. Coating. Technol.* 425 (2021) 127748, <https://doi.org/10.1016/j.surfcoat.2021.127748>.
- [15] Y. Xu, W. Li, L. Qu, X. Yang, B. Song, R. Lupoi, S. Yin, Solid-state cold spraying of FeCoCrNiMn high-entropy alloy: an insight into microstructure evolution and oxidation behavior at 700–900 °C, *J. Mater. Sci. Technol.* 68 (2021) 172–183, <https://doi.org/10.1016/j.jmst.2020.06.041>.
- [16] T. Schmidt, H. Assadi, F. Gärtner, H. Richter, T. Stoltenhoff, H. Kreye, T. Klassen, From particle acceleration to impact and bonding in cold spraying, *J. Therm. Spray Technol.* 18 (2009) 794–808, <https://doi.org/10.1007/s11666-009-9357-7>.
- [17] M. Kamaraj, V.M. Radhakrishnan, Cold spray coating diagram: bonding properties and construction methodology, *J. Therm. Spray Technol.* 28 (2019), <https://doi.org/10.1007/s11666-019-00853-5>.
- [18] M. Gruijicic, C.L. Zhao, W.S. DeRosset, D. Helfritch, Adiabatic shear instability based mechanism for particles/substrate bonding in the cold-gas dynamic-spray process, *Mater. Des.* 25 (2004), <https://doi.org/10.1016/j.matdes.2004.03.008>.
- [19] M. Kamaraj, V.M. Radhakrishnan, Cold spray coating diagram: bonding properties and construction methodology, *J. Therm. Spray Technol.* 28 (2019) 756–768, <https://doi.org/10.1007/s11666-019-00853-5>.
- [20] J. Karthikyan, The advantages and disadvantages of the cold spray coating process, *Cold Spray Mater. Depos. Proc. Fundam. Appl.* (2007) 62–71, <https://doi.org/10.1533/9781845693787.1.62>.
- [21] M.F. Smith, S.N. Laboratories, Introduction to cold spray, in: High Press. Cold Spray, 2020, pp. 1–16, <https://doi.org/10.31399/asm.tb.hpcspa.t54460001>.
- [22] A. Anupam, S. Kumar, N.M. Chavan, B.S. Murty, R.S. Kottada, First report on cold-sprayed AlCoCrFeNi high-entropy alloy and its isothermal oxidation, *J. Mater. Res.* 34 (2019) 796–806, <https://doi.org/10.1557/jmr.2019.38>.
- [23] J.E. Ahn, Y.K. Kim, S.H. Yoon, K.A. Lee, Tuning the microstructure and mechanical properties of cold sprayed equiatomic CoCrFeMnNi high-entropy alloy coating layer, *Met. Mater. Int.* (2020), <https://doi.org/10.1007/s12540-020-00886-4>.
- [24] A. Concustell, J. Henao, S. Dosta, N. Cinca, I.G. Cano, J.M. Guilemany, On the formation of metallic glass coatings by means of Cold Gas Spray technology, *J. Alloys Compd.* 651 (2015) 764–772, <https://doi.org/10.1016/j.jallcom.2015.07.270>.
- [25] A. List, F. Gärtner, T. Schmid, T. Klassen, Impact conditions for cold spraying of hard metallic glasses, *J. Therm. Spray Technol.* 21 (2012) 531–540, <https://doi.org/10.1007/s11666-012-9750-5>.
- [26] X. Li, Additive manufacturing of advanced multi-component alloys: bulk metallic glasses and high entropy alloys, *Adv. Eng. Mater.* 20 (2018) 1–18, <https://doi.org/10.1002/adem.201700874>.
- [27] J. Afti, H. Okazaki, M. Yamada, M. Fukumoto, Fabrication of aluminum coating onto CFRP substrate by cold spray, *Mater. Trans.* 52 (2011) 1759–1763, <https://doi.org/10.2320/matertrans.T-M2011807>.
- [28] S.L. Fu, C.X. Li, Y.K. Wei, X.T. Luo, G.J. Yang, C.J. Li, J.L. Li, Novel method of aluminum to copper bonding by cold spray, *J. Therm. Spray Technol.* 27 (2018), <https://doi.org/10.1007/s11666-018-0707-1>.
- [29] J.G. Legoux, E. Irissou, C. Moreau, Effect of substrate temperature on the formation mechanism of cold-sprayed aluminum, zinc and tin coatings, *J. Therm. Spray Technol.* 16 (2007) 619–626, <https://doi.org/10.1007/s11666-007-9091-y>.
- [30] M. Fukumoto, H. Terada, M. Mashiko, K. Sato, M. Yamada, E. Yamaguchi, Deposition of copper fine particle by cold spray process, *Mater. Trans.* 50 (2009) 1482–1488, <https://doi.org/10.2320/matertrans.MRA2008223>.
- [31] M. Doubenskaia, Y.S. Latifulina, M.N. Samodurova, Cold spray deposition of copper/tungsten composite coatings, *IOP Conf. Ser. Mater. Sci. Eng.* 969 (2020), <https://doi.org/10.1088/1757-899X/969/1/012106>.
- [32] H. Koivuluoto, M. Honkanen, P. Vuoristo, Cold-sprayed copper and tantalum coatings - detailed FESEM and TEM analysis, *Surf. Coating. Technol.* 204 (2010) 2353–2361, <https://doi.org/10.1016/j.surfcoat.2010.01.001>.
- [33] C.J. Li, W.Y. Li, Deposition characteristics of titanium coating in cold spraying, *Surf. Coating. Technol.* 167 (2003) 278–283, [https://doi.org/10.1016/S0257-8972\(02\)00919-2](https://doi.org/10.1016/S0257-8972(02)00919-2).
- [34] T.S. Price, P.H. Shipway, D.G. McCartney, Effect of cold spray deposition of a titanium coating on fatigue behavior of a titanium alloy, *Proc. Int. Therm. Spray Conf.* 15 (2006) 507–512, <https://doi.org/10.1361/105996306X147108>.
- [35] M. Jahedi, S. Zahiri, S. Gulizia, B. Tiganis, C. Tang, D. Fraser, Direct manufacturing of titanium parts by cold spray, *Mater. Sci. Forum* 618 619 (2009) 505–508, <https://doi.org/10.4028/www.scientific.net/MSF.618-619.505>.
- [36] N.I. Omar, S. Selvam, M. Kaisho, M. Yamada, T. Yasui, M. Fukumoto, Deposition of titanium dioxide coating by the cold-spray process on annealed stainless steel substrate, *Coatings* 10 (2020) 1–13, <https://doi.org/10.3390/coatings10100991>.
- [37] D. MacDonald, R. Fernández, F. Delloro, B. Jodoin, Cold spraying of armstrong process titanium powder for additive manufacturing, *J. Therm. Spray Technol.* 26 (2017) 598–609, <https://doi.org/10.1007/s11666-016-0489-2>.
- [38] H. Koivuluoto, J. Lagerbom, P. Vuoristo, Microstructural studies of cold sprayed copper, nickel, and nickel-30% copper coatings, *J. Therm. Spray Technol.* 16 (2007) 488–497, <https://doi.org/10.1007/s11666-007-9060-5>.
- [39] M. Winnicki, S. Kozerski, A. Małachowska, L. Pawłowski, M. Rutkowska-Gorczyca, Optimization of ceramic content in nickel-alumina composite coatings obtained by low pressure cold spraying, *Surf. Coating. Technol.* 405 (2021), <https://doi.org/10.1016/j.surfcoat.2020.126732>.
- [40] R. Della Gatta, A. Viscusi, A.S. Perna, A. Caraviello, A. Astarita, Feasibility of steel powder deposition on composites through cold spray, *Mater. Manuf. Process.* 36 (2021), <https://doi.org/10.1080/10426914.2020.1832693>.
- [41] K. Spencer, M.X. Zhang, Optimisation of stainless steel cold spray coatings using mixed particle size distributions, *Surf. Coating. Technol.* 205 (2011), <https://doi.org/10.1016/j.surfcoat.2011.05.020>.
- [42] B. Al-Mangour, R. Mongrain, E. Irissou, S. Yue, Improving the strength and corrosion resistance of 316L stainless steel for biomedical applications using cold spray, *Surf. Coating. Technol.* 216 (2013) 297–307, <https://doi.org/10.1016/j.surfcoat.2012.11.061>.
- [43] J. Tang, SiC P/Al5056 Composite Coatings Applied to A Magnesium Substrate by Cold Gas Dynamic Spray and, 2020.
- [44] X.K. Suo, X.P. Guo, W.Y. Li, M.P. Planche, H.L. Liao, Investigation of deposition behavior of cold-sprayed magnesium coating, *J. Therm. Spray Technol.* 21 (2012) 831–837, <https://doi.org/10.1007/s11666-012-9777-7>.
- [45] F.F. Lu, K. Ma, C.X. Li, M. Yasir, X.T. Luo, C. jiu Li, Enhanced corrosion resistance of cold-sprayed and shot-peened aluminum coatings on LA43M magnesium alloy, *Surf. Coating. Technol.* 394 (2020) 125865, <https://doi.org/10.1016/j.surfcoat.2020.125865>.
- [46] H.J. Kim, C.H. Lee, S.Y. Hwang, Superhard nano WC-12%Co coating by cold spray deposition, *Mater. Sci. Eng. A.* 391 (2005) 243–248, <https://doi.org/10.1016/j.msea.2004.08.082>.
- [47] M. Yandouzi, L. Ajedlsztajn, B. Jodoin, WC-based composite coatings prepared by the pulsed gas dynamic spraying process: effect of the feedstock powders, *Surf. Coating. Technol.* 202 (2008) 3866–3877, <https://doi.org/10.1016/j.surfcoat.2008.01.036>.
- [48] H.J. Kim, C.H. Lee, S.Y. Hwang, Fabrication of WC-Co coatings by cold spray deposition, *Surf. Coating. Technol.* 191 (2005) 335–340, <https://doi.org/10.1016/j.surfcoat.2004.04.058>.
- [49] S. Yin, W. Li, B. Song, X. Yan, M. Kuang, Y. Xu, K. Wen, R. Lupoi, Deposition of FeCoNiCrMn high entropy alloy (HEA) coating via cold spraying, *J. Mater. Sci. Technol.* 35 (2019) 1003–1007, <https://doi.org/10.1016/j.jmst.2018.12.015>.
- [50] Y. Xu, W. Li, L. Qu, X. Yang, B. Song, R. Lupoi, S. Yin, Solid-state cold spraying of FeCoCrNiMn high-entropy alloy: an insight into microstructure evolution and oxidation behavior at 700–900 °C, *J. Mater. Sci. Technol.* (2020), <https://doi.org/10.1016/j.jmst.2020.06.041>.
- [51] J. Lehtonen, H. Koivuluoto, Y. Ge, A. Juselius, S.P. Hannula, Cold gas spraying of a high-entropy CrFeNiMn equiatomic alloy, *Coatings* 10 (2020), <https://doi.org/10.3390/coatings10010053>.
- [52] Y. Zhang, T. Bian, X. Shen, Z. Wang, S. Ye, S. Feng, K. Yu, C. Ding, P. Yu, Sintering mechanism and microstructure evolution of a CoCrFeNiMn high entropy alloy fabricated by metal injection molding, *J. Alloys Compd.* 868 (2021) 158711, <https://doi.org/10.1016/j.jallcom.2021.158711>.
- [53] K. Ren, H. Liu, R. Chen, Y. Tang, B. Guo, S. Li, J. Wang, R. Wang, F. Lu, A Compression properties and impact energy release characteristics of TiZrNbV high-entropy alloy, *Mater. Sci. Eng. A.* 827 (2021) 142074, <https://doi.org/10.1016/j.msea.2021.142074>.
- [54] R. Liu, Y. Jiao, Y. Guo, L. Chen, Z. Li, A. Sha, F. Gao, P. Chen, Dynamic behavior and microstructural evolution of TiAl alloys tailored via phase and grain size, *J. Mater. Res. Technol.* 22 (2023) 292–306, <https://doi.org/10.1016/j.jmrt.2022.11.109>.
- [55] G.K. Williamson, W.H. Hall, X-ray line broadening from filed aluminium and wolfram, *Acta Metall.* 1 (1953) 22–31, [https://doi.org/10.1016/0001-6160\(53\)90006-6](https://doi.org/10.1016/0001-6160(53)90006-6).
- [56] D.F. Rojas, H. Li, O.K. Orhan, C. Shao, J.D. Hogan, M. Ponga, Mechanical and microstructural properties of a CoCrFe0.75NiMo0.3Nb0.125 high-entropy alloy additively manufactured via cold-spray, *J. Alloys Compd.* 893 (2022) 162309, <https://doi.org/10.1016/j.jallcom.2021.162309>.
- [57] J.Y. He, H. Wang, H.L. Huang, X.D. Xu, M.W. Chen, Y. Wu, X.J. Liu, T.G. Nieh, K. An, Z.P. Lu, A precipitation-hardened high-entropy alloy with outstanding tensile properties, *Acta Mater.* 102 (2016) 187–196, <https://doi.org/10.1016/j.actamat.2015.08.076>.
- [58] S.I. Wright, M.M. Nowell, D.P. Field, A review of strain analysis using electron backscatter diffraction, *Microsc. Microanal.* 17 (2011) 316–329, <https://doi.org/10.1017/S1431927611000055>.
- [59] A. Puglione, B. Dovgyy, C. Liu, C.M. Gourlay, P.A. Hooper, M.S. Pham, Printability and microstructure of the CoCrFeMnNi high-entropy alloy fabricated by laser powder bed fusion, *Mater. Lett.* 224 (2018) 22–25, <https://doi.org/10.1016/j.mattlet.2018.04.052>.
- [60] C. Haase, F. Tang, M.B. Wilms, A. Weisheit, B. Hallstedt, Combining thermodynamic modeling and 3D printing of elemental powder blends for high-throughput investigation of high-entropy alloys – towards rapid alloy screening and design, *Mater. Sci. Eng. A.* 688 (2017) 180–189, <https://doi.org/10.1016/j.msea.2017.01.099>.

- [61] M.J. Jang, S.H. Joo, C.W. Tsai, J.W. Yeh, H.S. Kim, Compressive deformation behavior of CrMnFeCoNi high-entropy alloy, *Met. Mater. Int.* 22 (2016) 982–986, <https://doi.org/10.1007/s12540-016-6304-2>.
- [62] N.L. Okamoto, S. Fujimoto, Y. Kambara, M. Kawamura, Z.M.T. Chen, H. Matsunoshita, K. Tanaka, H. Inui, E.P. George, Size effect, critical resolved shear stress, stacking fault energy, and solid solution strengthening in the CrMnFeCoNi high-entropy alloy, *Sci. Rep.* 6 (2016) 1–10, <https://doi.org/10.1038/srep35863>.
- [63] Q. Cheng, X.D. Xu, X.Q. Li, Y.P. Li, T.G. Nieh, M.W. Chen, Solid solution softening in a Al0.1CoCrFeMnNi high-entropy alloy, *Scripta Mater.* 186 (2020) 63–68, <https://doi.org/10.1016/j.scriptamat.2020.04.034>.
- [64] N.D. Stepanov, D.G. Shaysultanov, N.Y. Yurchenko, S.V. Zherebtsov, A.N. Ladygin, G.A. Salishchev, M.A. Tikhonovsky, High temperature deformation behavior and dynamic recrystallization in CoCrFeNiMn high entropy alloy, *Mater. Sci. Eng. A.* 636 (2015) 188–195, <https://doi.org/10.1016/j.msea.2015.03.097>.
- [65] N. Ansari, B. Tran, W.J. Poole, S.S. Singh, H. Krishnaswamy, J. Jain, High temperature deformation behavior of Mg-5wt.%Y binary alloy: constitutive analysis and processing maps, *Mater. Sci. Eng. A.* 777 (2020) 139051, <https://doi.org/10.1016/j.msea.2020.139051>.
- [66] H. Wen, T.D. Topping, D. Isheim, D.N. Seidman, E.J. Lavernia, Strengthening mechanisms in a high-strength bulk nanostructured Cu-Zn-Al alloy processed via cryomilling and spark plasma sintering, *Acta Mater.* 61 (2013) 2769–2782, <https://doi.org/10.1016/j.actamat.2012.09.036>.
- [67] S.J. Sun, Y.Z. Tian, H.R. Lin, H.J. Yang, X.G. Dong, Y.H. Wang, Z.F. Zhang, Transition of twinning behavior in CoCrFeMnNi high entropy alloy with grain refinement, *Mater. Sci. Eng. A.* 712 (2018) 603–607, <https://doi.org/10.1016/j.msea.2017.12.022>.
- [68] F. Otto, A. Dlouhý, C. Somsen, H. Bei, G. Eggeler, E.P. George, The influences of temperature and microstructure on the tensile properties of a CoCrFeMnNi high-entropy alloy, *Acta Mater.* 61 (2013) 5743–5755, <https://doi.org/10.1016/j.actamat.2013.06.018>.
- [69] S. Lyu, G. Li, R. Zheng, W. Xiao, Y. Huang, N. Hort, M. Chen, C. Ma, Reduced yield asymmetry and excellent strength-ductility synergy in Mg-Y-Sm-Zn-Zr alloy via ultra-grain refinement using simple hot extrusion, *Mater. Sci. Eng. A.* 856 (2022) 143783, <https://doi.org/10.1016/j.msea.2022.143783>.
- [70] Z. Wu, H. Bei, G.M. Pharr, E.P. George, Temperature dependence of the mechanical properties of equiatomic solid solution alloys with face-centered cubic crystal structures, *Acta Mater.* 81 (2014) 428–441, <https://doi.org/10.1016/j.actamat.2014.08.026>.
- [71] B.R. Chen, A.C. Yeh, J.W. Yeh, Effect of one-step recrystallization on the grain boundary evolution of CoCrFeMnNi high entropy alloy and its subsystems, *Sci. Rep.* 6 (2016) 1–9, <https://doi.org/10.1038/srep22306>.
- [72] W.H. Liu, Y. Wu, J.Y. He, T.G. Nieh, Z.P. Lu, Grain growth and the Hall-Petch relationship in a high-entropy FeCrNiCoMn alloy, *Scripta Mater.* 68 (2013) 526–529, <https://doi.org/10.1016/j.scriptamat.2012.12.002>.
- [73] P. Zhang, S.X. Li, Z.F. Zhang, General relationship between strength and hardness, *Mater. Sci. Eng. A.* 529 (2011) 62–73, <https://doi.org/10.1016/j.msea.2011.08.061>.
- [74] H.L. Zhang, D.D. Cai, X. Sun, H. Huang, S. Lu, Y.Z. Wang, Q.M. Hu, L. Vitos, X. D. Ding, Solid solution strengthening of high-entropy alloys from first-principles study, *J. Mater. Sci. Technol.* 121 (2022) 105–116, <https://doi.org/10.1016/j.jmst.2021.11.076>.
- [75] K. Yang, W. Li, X. Yang, Y. Xu, A. Vairis, Effect of heat treatment on the inherent anisotropy of cold sprayed copper deposits, *Surf. Coating. Technol.* 350 (2018) 519–530, <https://doi.org/10.1016/j.surfcoat.2018.07.046>.
- [76] S. Yin, R. Jenkins, X. Yan, R. Lupoi, Microstructure and mechanical anisotropy of additively manufactured cold spray copper deposits, *Mater. Sci. Eng. A.* 734 (2018) 67–76, <https://doi.org/10.1016/j.msea.2018.07.096>.
- [77] S.E. Julien, A. Nourian-avval, W. Liang, T. Schwartz, O.C. Ozdemir, S. Müftü, Bulk fracture anisotropy in Cold-Sprayed Al 6061 deposits, *Eng. Fract. Mech.* 263 (2022) 108301, <https://doi.org/10.1016/j.engfracmech.2022.108301>.